Industrial Mathematics and Statistical Modeling Workshop for Graduate Students, July 26 - August 3, 2004

Edited by H.T. Banks, Pierre Gremaud, Negash G.Medhin, and Ralph C. Smith.

Participants

Graduate Students

1. Almond, Natalie, Western California University
2. An, Jung-Ha, University of Florida
3. Boubakari, Ibrahimou, University of South Florida
4. Breen, Miyuki, Case Western Reserve University
5. Burgess, Richard, University of Tennessee
6. Chen, Zheng, Florida State University
7. Cheng, Jing, Purdue University
8. Ding, Wandi, University of Tennessee
9. Ettinger, Bree, University of Georgia
10. Fernando, Harshini, Texas Tech University
11. Hariharanath, Kavuri, University of Tennessee
12. Jackson, Billy, University of Georgia
13. Kandala, Sampath, University of Tennessee
14. Khoujmane, Ali, Texas Tech University
15. Li, Xiaochuan, University of Mississippi
16. Liu, Xingtao, SUNY
17. Liu, Yuan, UNC Wilmington
18. Nandi, Subhrangshu, University of Massachusetts
19. Ramirez, Ismael, UAM-I
20. Ren, Kui, Columbia University
21. Rothstein, Ivan, Virginia Tech
22. Rusnica, Steven, Allegheny College/NCSU
23. Santos, Brenda, Centro de Investigacion en Matematicas
24. Sweetingham, Kelly, Auburn University/NCSU
25. Vaughan, Tamara, University of Alabama

26. Walker, Matthew, Texas Tech University
27. Ward, Carrie, NC State University
28. Wilder, Mike, UNC-Greensboro
29. Wilson, Heather, U. of Central Florida/NCSU
30. Wu, Meng, UNC-Wilmington

Problem Presenters

1. Hicks, Gregory, AFRL/VSSV
2. Horton, Michael C. and Choi, Melissa, Massachusetts Institute of Technology, Lincoln Laboratory
3. Ives, Lawrence, Calabazas Creek Research, Inc.
4. Jarabek, Annie M., Sclosser, Paul and Wong, Brian, CIIT Centers for Health Research
5. Maldague, Pierre, Jet Propulsion Laboratory
6. Trussel, H. Joel, Electrical and Computer Engineering, NCSU

Faculty Advisors

1. Buche, Robert
2. Haider, Mansoor
3. Ito, Kazi
4. Lada, Emily
5. Li, Zhilin
6. Olufson, Mette
7. Pang, Tao
8. Tran, Hien
9. Zenkov, Dimitri

Contents

Preface

This volume contains the proceedings of the Industrial Mathematical and Statistical Modeling Workshop for Graduate Students that was held at the Center for Research in Scientific Computation at North Carolina State University (NCSU), Raleigh, North Carolina, July 26 - August 3, 2003. This workshop which was the tenth one held at NCSU brought together 30 graduate students. These students represented a large number of graduate programs including Allegheny College, Auburn University, Case Western Reserve University, Centro de Investigacion en Matematicas, Columbia University, Florida State University, North Carolina State University, Purdue University, SUNY, Texas Tech University UAM-I University of Alabama, University of Central Florida, University of Florida, University of Georgia, University of Massachusetts University of S Mississippi University of North Carolina-Greensboro, University of North Carolina-Wilmington, University of South Florida, University of Tennessee, Virginia Tech Western Carolina University.

The students were divided into five teams to work on "industrial mathematics" problems presented by industrial scientists. These were not the neat, well-posed academic exercises typically found in coursework, but were challenging real world problems from industry or applied science. The problems, which were presented to the students on the first day of the workshop, required fresh insights for their formulation and solution. Each group spent the first eight days of the workshop investigating their project and then reported their findings in half-hour public seminars on the last day of the workshop.

The following is a list of the presenters and the projects they brought to the workshop.

- **Gregory Hicks** (AFRL/VSSV) *The Unifying of Perspective on Attitude and Shape Control*
- **Michael C. Horton** (Massachusetts Institute of Technology, Lincoln Laboratory) *Mobile Sensing of Aerosolized Chemical and Biological Agents*
- **Lawrence Ives** (Calabazas Creek Research, Inc.) *Optimized Design of Electron Guns for High Power RF Applications*
- **Pierre Maldague** (Jet Propulsion Laboratory) *Estimating the Complexity of Event-Driven Command Sequences Executing in Parallel*
- **Paul Schlosser, Brian Wang, Annie M. Jarabek** (CIIT Centers for Health Research), **H. Joel Trussel** (Electrical and Computer Engineering, NCSU) *Identifying Respiratory Parameters from Plethysmography Data*

These problems represent a broad spectrum of mathematical topics and applications. Although nine days is a short time for a full investigation of some of the aspects of such industrial problems, the reader will observe remarkable progress on all projects.

We, the organizers, strongly believe that this type of workshop provide very valuable non-academic research related experiences for graduate students while contributing to the research efforts of industrial participants. In addition, this type of activity facilitates the development of graduate students' ability to communicate and interact with scientists who are not traditional mathematicians but require and employ mathematical tools in their work. By providing a unique experience of how Mathematics is applied outside Academia, the workshop has helped many students in deciding what kind of career they aspire to. In some cases in past workshops, this help has been in the form of direct hiring by the participating companies. By broadening the horizon beyond what is usually presented in graduate education, students interested in academic careers also find a renewed sense of excitement about Applied Mathematics.

The success of the workshop was greatly enhanced by active participation in a very friendly atmosphere and almost uninterrupted work during the nine days of attendance. The organizers are most grateful to participants for their contributions. Funding for the workshop was provided by the Statistical and Applied Mathematical Sciences Institute (SAMSI) with additional financial support, personnel, and facilities provided by the Center for Research in Scientific Computation (CRSC) and the Department of Mathematics at North Carolina State University. Finally, we would like to thank Brenda Currin, Kathleen McGowan, Lesa Denning, and Rory Schnell for their efforts and help in all administrative matters. We are also grateful to Brian Adams, Brandy Benedict, Nathan Gibson and Jeff Hood for their help in providing transportation, setting up computer accounts, and many other ways that made the workshop a success.

H.T. Banks, Pierre Gremaud, Negash G. Medhin, Ralph Smith
Raleigh, 2004.

Chapter 1

PROBLEM 1: The Unifying of Perspective on Attitude and Shape Control

Jung-ha An[1], Ibrahimou Boubakari[2], Richard Burgess[3],

Billy Jackson[4], Hariharanath Kavuri[5], Matthew Walker[6]

Problem Presenter:
Gregory Hicks
AFRL/VSSV

The issues surrounding the use of overdetermined parameterizations of the 1-sphere in the formulation of governing equations of motion and control design for mechanical systems evolving on this manifold are addressed by means of an example. When modeling, the introduction and subsequent elimination of the Lagrange multiplier leads to numerical drift. An approach to eliminating this drift is introduced. The typical design of a controller is made indirect by coordinate redundancy. This issue is obviated by designing in a chart and then translating the result via coordinate transformations. The intent is to liken the findings to the analogous situation presented by the 3-sphere parameterization of the rotation group.

1.1 Problem Statement and Motivation

The task we are taking up is to provide a proper examination of the Lie group SO_3 in the context of dynamics and control formulation. This classical linear group naturally arises as a configuration space, or a component thereof, when mathematically treating dynamics of a spacecraft.

When stating equations of motion and developing attitude or shape controls a coordinate approach is often taken. This leads to issues in this particular case on account of the fact that SO_3 has no global chart. To circumvent this issue it is typical to make use of the unit quaternions in establishing a global covering.

Due to dependencies amongst these coordinates a straightforward use of the Lagrangian program is not permissible and typical control approaches become contrived. In particular, we have in mind the use of output

[1]University of Florida
[2]University of South Florida
[3]University of Tennessee
[4]University of Georgia
[5]University of Tennessee
[6]Texas Tech University

feedback linearization as well as its variants. However, dynamics and control are geometric in nature and are thus independent of choice of coordinates. Hence, it seems fair to say that it is unseemly to generate a huge body of literature dedicated to arriving at what is philosophically the same controller from a multitude of coordinates perspectives, proclaiming in each instance to have developed something new.

We wish to establish to what extent we may elucidate from a single control philosophy in SO_3, expressions of controllers which make use of standard coordinate systems such as the unit quaternions.

1.2 Introduction

In this paper we aid the cause issued per the problem statement by examining the potentials and aside issues of readily obtaining what is desired for SO_3 by looking at an analogous problem, that of working on the circle S^1. In particular, we take up the study of dynamics and control of a simple pendulum. We experiment with the ramifications of using over-determined coordinates on S^1 in the settings of dynamics and control. Specifically, we expose numerical conundrums linked to the field of DAE's (Differential Algebraic Equations) and indicate how one may elicit controllers in this setting from those designed in a natural coordinate setting.

1.3 The Dynamics of an Inverted Pendulum

In this section, we consider the dynamics of the simple inverted pendulum. We develop the governing equations of motion in the context of two parameterizations of S^1. The first taken up is the angle measure parameterization. The second shall be the cartesian coordinate parameterization naturally induced by immersing S^1 into E^2. In both instances we employ the Lagrangian perspective.

1.3.1 The Angle Measure Parameterization

Consider a bob type inverted pendulum. The bob is connected to the fixed point of rotation by means of a virtually massless rod. The mechanical Lagrangian L of the system is the difference between the kinetic energy K and potential energy U: $L = K - U$, $K = \frac{1}{2}mv^2$, and $U = mgh$. Here m is the bob's mass, g is magnitude of acceleration due to gravity, v is velocity, and h is the relative height of the bob. Let θ denote the clockwise angle measure of the pendulum's displacement from its inverted configuration. Then, $v = r\omega$, where ω is the scalar function determining angular velocity. Hence the Lagrangian is

$$L = \frac{1}{2}mr^2\dot{\theta}^2 - mgr\cos(\theta).$$

The equation of motion for the pendulum system is given by the Euler–Lagrange equation

$$\frac{d}{dt}\frac{\partial L}{\partial \dot{\theta}} - \frac{\partial L}{\partial \theta} = 0.$$

Hence we have

$$mr^2\ddot{\theta} - mgr\sin(\theta) = 0. \tag{1.1}$$

Examination of the potential indicates, upon identification, that there are two configurations of equilibria, corresponding to $\theta = 0, \pi$. The first of these is the unstable upward vertical configuration and the second, the stable downward vertical configuration. The system, being devoid of damping, is Hamiltonian. Since the system is Hamiltonian and the number of degrees of freedom equals 1, all phase space trajectories correspond to the level sets of the Hamiltonian $H = K + U$, given by the Lagendre transform of L.

1.3.2 The Cartesian Coordinate Parameterization

Next, we over-parameterize the configuration space of the system by means of the immersion

$$q_1 = \sin(\theta),$$

$$q_2 = \cos(\theta)$$

of S^1 into E^2 and develop the equations of motion in Cartesian coordinates. In this case, the energies are expressed as

$$K = \frac{1}{2}mr^2(\dot{q}_1^2 + \dot{q}_2^2),$$
$$U = mgq_2.$$

Thus the Lagrangian is

$$L = \frac{1}{2}mr^2(\dot{q}_1^2 + \dot{q}_2^2) - mgrq_2.$$

As before we make use of the expressions

$$\frac{d}{dt}\frac{\partial L}{\partial \dot{q}_1} - \frac{\partial L}{\partial q_1} = mr^2\ddot{q}_1$$
$$\frac{d}{dt}\frac{\partial L}{\partial \dot{q}_2} - \frac{\partial L}{\partial q_2} = mr^2\ddot{q}_2 + mgr$$

generated from the Lagrangian in the determination of the governing equations of motion. However, here, we have the constraint $f(q_1, q_2) = 0$, $f(q_1, q_2) = q_1^2 + q_2^2 - 1 = 0$, indicating that the forces provided do not balance. Equilibrium is obtained only upon inclusion of the force of constraint, which being proportional to ∇f, is included by means of the Lagrange multiplier λ. Thus the dynamic behavior is governed by the DAEs

$$mr^2\ddot{q}_1 + \lambda q_1 = 0 \ , \tag{1.3a}$$

$$mr^2\ddot{q}_2 + mgr + \lambda q_2 = 0 \ , \tag{1.3b}$$

$$q_1^2 + q_2^2 - 1 = 0 \ , \tag{1.3c}$$

where we have allowed the multiplier to absorb the factor of 2 generated by the gradient.

A typical way to handle DAEs is to bring them into the form of a system of ODEs, eliminating the Lagrange multipliers through direct analytic differentiation of the constraint equations. We now expose this procedure as it applies to mechanical systems. We follow directly the presentation of Ascher and Petzold [9].

Mechanical systems may be written in the form

$$\dot{\mathbf{q}} = \mathbf{v} \ , \tag{1.4a}$$

$$M(\mathbf{q})\dot{\mathbf{v}} = \mathbf{f}(\mathbf{q}, \mathbf{v}) - G^{\mathrm{T}}(\mathbf{q})\boldsymbol{\lambda} \ , \tag{1.4b}$$

$$\mathbf{g}(\mathbf{q}) = \mathbf{q} \ , \tag{1.4c}$$

where $\mathbf{q}$ are curvilinear coordinates on the configuration space, $\mathbf{v} = \dot{\mathbf{q}}$, M is the system's generalized mass matrix, $\mathbf{f}$ the impressed force field, $G = \partial\mathbf{g}$, and $\mathbf{g}$ the constraint function vector. Two time differentiations of (1.4c) provide

$$\frac{\partial G\mathbf{v}}{\partial \mathbf{q}} = -G\dot{\mathbf{v}} \ . \tag{1.5}$$

Hence, upon multiplication of (1.4b) by GM^{-1}, one may determine that

$$\boldsymbol{\lambda}(\mathbf{q}, \mathbf{v}) = (GM^{-1}G^{\mathrm{T}})^{-1}\left(GM^{-1}\mathbf{f} + \frac{\partial G\mathbf{v}}{\partial \mathbf{q}}\right) \ . \tag{1.6}$$

Substituting this expression into (1.4b) provides us

$$\dot{\mathbf{q}} = \mathbf{v} \ , \tag{1.7a}$$

$$M(\mathbf{q})\dot{\mathbf{v}} = \mathbf{f}(\mathbf{q}, \mathbf{v}) - G^{\mathrm{T}}(\mathbf{q})(GM^{-1}G^{\mathrm{T}})^{-1}\left(GM^{-1}\mathbf{f} + \frac{\partial G\mathbf{v}}{\partial \mathbf{q}}\right) \ . \tag{1.7b}$$

Applying the process to the system at hand, it is determined that

$$\lambda = \frac{mr^2}{q_1^2 + q_2^2}\left(v_1^2 + v_2^2 - \frac{mgrq_2}{mr^2}\right) \ .$$

Thus (1.3a) and (1.3b) become

$$\dot{q}_1 = v_1 \ , \tag{1.8a}$$

$$\dot{q}_2 = v_2 \ , \tag{1.8b}$$

$$\dot{v}_1 = -\frac{1}{q_1^2 + q_2^2}\left(v_1^2 + v_2^2 - \frac{mgrq_2}{mr^2}\right) q_1 \ , \tag{1.8c}$$

$$\dot{v}_2 = -\frac{1}{q_1^2 + q_2^2}\left(v_1^2 + v_2^2 - \frac{mgrq_2}{mr^2}\right) q_2 - \frac{g}{r} \ . \tag{1.8d}$$

Accompanying this system of ODEs are the invariants:

$$q_1^2 + q_2^2 - 1 = 0$$
$$q_1 v_1 + q_2 v_2 = 0 \ .$$

1.4 Numerical Integration

Here we examine simulation results, comparing the outcomes obtained by means of the differing parameterizations. The results indicate that although systems (1.1) and (1.8) represent the same physical scenario, numerically they behave quite differently.

1.4.1 The Problems

We begin with (1.1). Taking $m = r = 1$ and $g = 9.8$ the system was integrated via the *MATLAB* routine **ode23s**. The results are presented in figure 1.1. As expected, one obtains a closed loop trajectory in phase space corresponding to the periodic motion of the pendulum. Now, consider (1.8). Using the same model

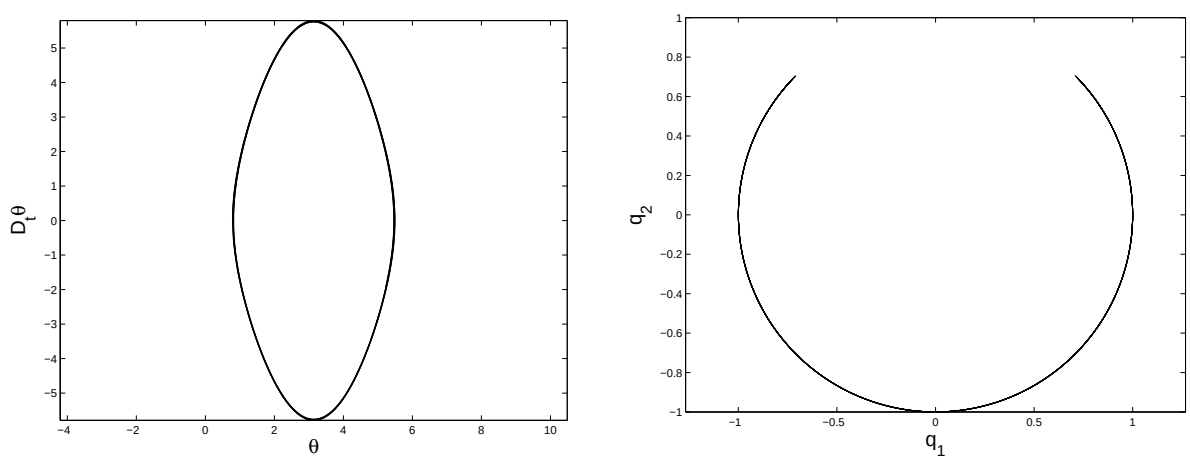

(a) θ phase

(b) configuration

Figure 1.1: Simulation results corresponding to the angle measure parameterization of the inverted pendulum.

parameters and numerical integration scheme we obtain the results seen in column 1 of figure 1.2. In this instance, an unacceptable drift is observed. The numerics do not respect the constraints of the system.

This outcome is not altogether unexpected, for the system we are dealing with is Hamiltonian and thus cannot be asymptotically stable. This makes the system at most marginally stable with respect to numerical integration even though the system may be stable. Putting this another way, the eigenvalues of a Hamiltonian system cannot lie strictly within $\mathbb{C}_0^-$ [8]. Thus, perturbations about the actual solution have the potential to grow without bound. Here, apparently, which situation we obtain, stable or unstable numerics, is quite coordinate dependent.

To illustrate just how sensitive the situation is, we consider making use of the following system:

$$\dot{q}_1 = v_1 \ , \tag{1.9a}$$

$$\dot{q}_2 = v_2 \ , \tag{1.9b}$$

$$\dot{v}_1 = -\left(v_1^2 + v_2^2 - \frac{mgrq_2}{mr^2}\right) q_1 \ , \tag{1.9c}$$

$$\dot{v}_2 = -\left(v_1^2 + v_2^2 - \frac{mgrq_2}{mr^2}\right) q_2 - \frac{g}{r} \ . \tag{1.9d}$$

Here we've taken system (1.8) but have observed the invariant $q_1^2 + q_2^2 - 1 = 0$. The results of numerical simulation are provided in column 2 of figure 1.2. In this instance we digress from a somewhat stable propagation of error to absolute instability.

1.4.2 Possible Solutions

Here we present possible solutions to the numerical issues which arise with redundant parameterization of a system's configuration space. There are two common techniques employed, namely, *projection* and *attenuation*. We shall illustrate the former along with a non-standard, however, exceedingly more natural, procedure, determined during our study of this issue [7].

The idea of projection requires little explanation. Should the numerical integration scheme employed not respect the constraints of the system defining its configuration manifold, then we project the state onto the manifold at each time step and use this projection in the evaluation of velocity fields. In the case of S^1 immersed in E^2, the projection is simple, the state vector $\mathbf{q}$ is normalized, placing it back onto S^1.

We illustrate with system (1.8). The results of integration with renormalization are provided in column 1 of figure 1.3. The results are encouraging. Indeed, upon renormalization, one observes only a small drift in the phase flows of the Cartesian coordinates and the errors in the configuration space are difficult to perceive. Apparently, one could destroy the drift completely if the projections were to be taken as the state approximates in an outright manner.

We now illustrate a technique which, in part, obviates the need for such "manual correction" techniques, or, at least, makes their application appear closer to appropriate. The idea is based on the observation that the numerical drift observed is *due to the two differentiations* used to reformulate the index 2 DAE into a system of ODEs (see [9] for an explanation). Thus, a preferred approach would be to eliminate the Lagrange multiplier by algebraic means. This can in fact be done in certain circumstances and the process is illustrated for the system at hand.

For ease of illustration and definiteness, let $m = r = 1$, as in the numerical simulation. Then (1.3a) and (1.3b) become

$$\dot{v}_1 = -\lambda q_1 \ , \tag{1.10a}$$

$$\dot{v}_2 = -\lambda q_2 - g \ , \tag{1.10b}$$

Scaling the former by $-q_2$, and the latter by q_1, and adding the resulting equations yields

$$q_2 \dot{v}_1 - q_1 \dot{v}_2 = q_1 g \ . \tag{1.11}$$

The left-hand side of this expression is recognized to be the rate of change of angular momentum $\dot{p}$. Further $v_1 = pq_2$ and $v_2 = -pq_1$. Thus, we arrive at the system

$$\dot{p} = gq_1 \ , \tag{1.12a}$$

$$v_1 = pq_2 \ , \tag{1.12b}$$

$$v_2 = -pq_1 \ , \tag{1.12c}$$

both simple and eloquent. However, the important distinction to make is that we eliminated the multiplier without differentiation.

[7] This method is properly to be credited to Dmitry Zenkov.

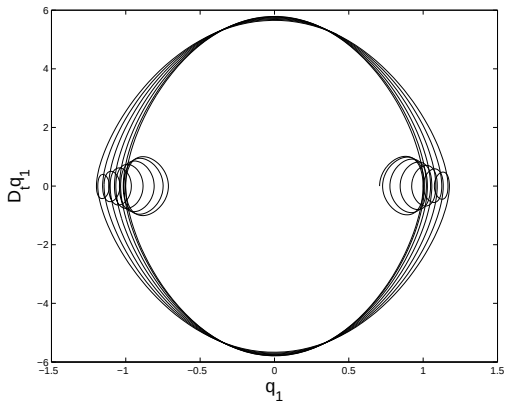

(a) q_1 phase

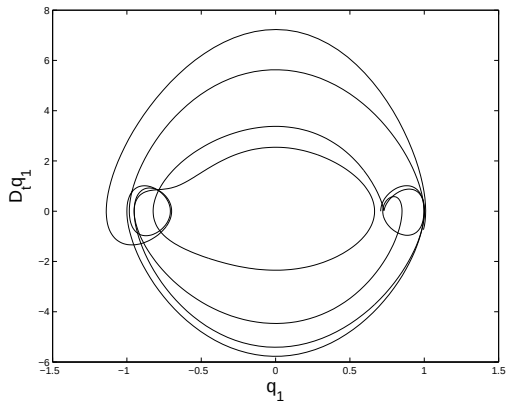

(b) q_1 phase

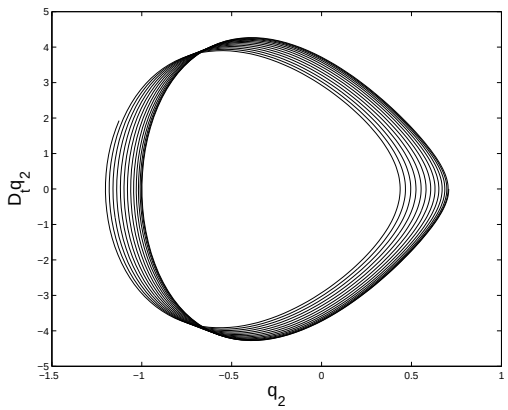

(c) q_2 phase

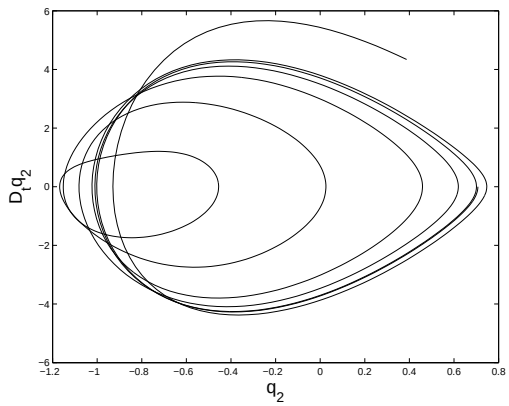

(d) q_2 phase

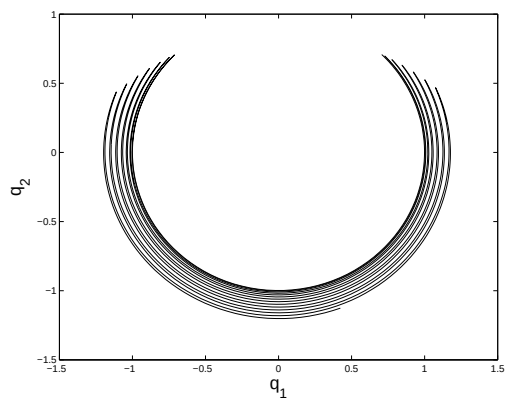

(e) configuration

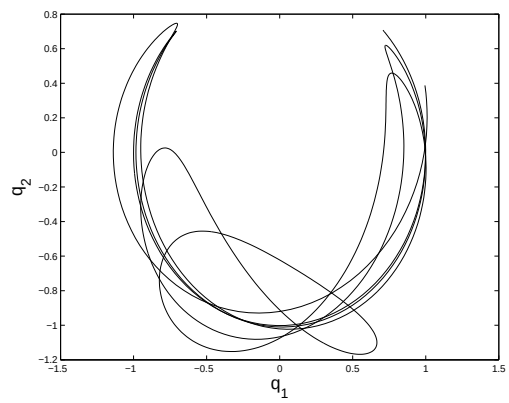

(f) configuration

Figure 1.2: Phase and Configuration Plots: Systems (1.8) (column 1) and (1.9) (column 2).

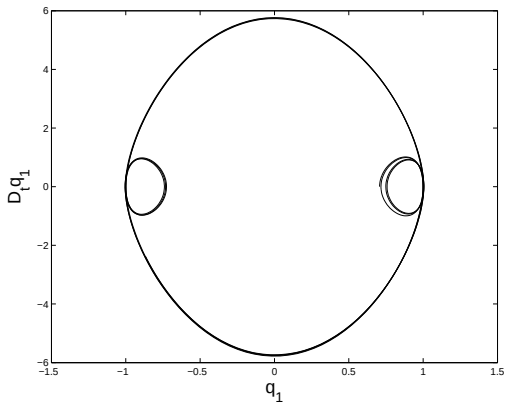

(a) q_1 phase

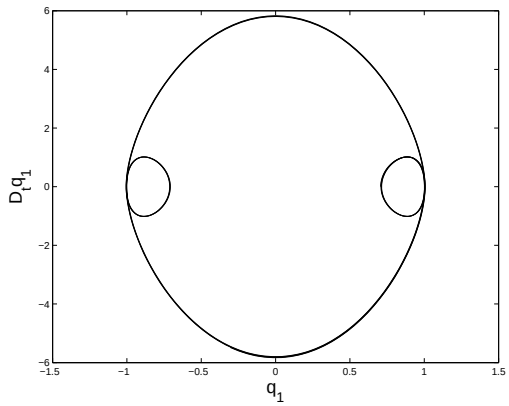

(b) q_1 phase

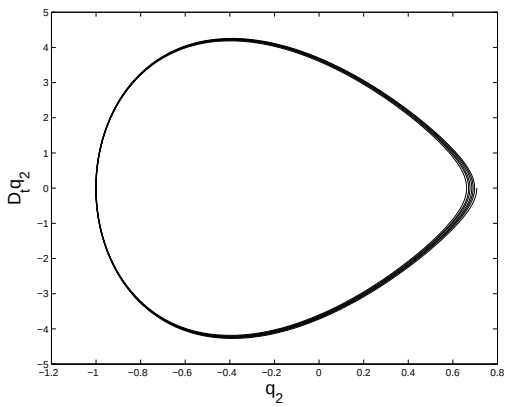

(c) q_2 phase

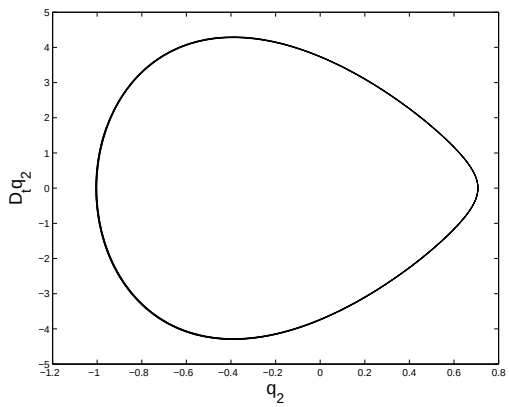

(d) q_2 phase

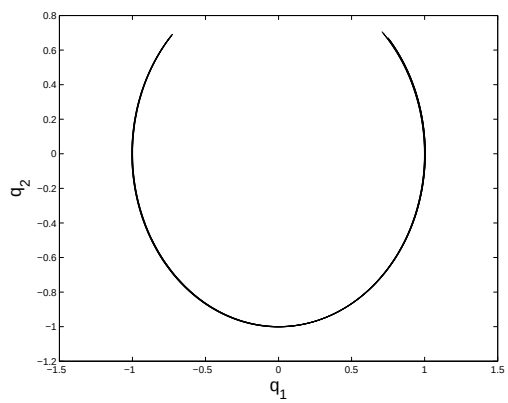

(e) configuration

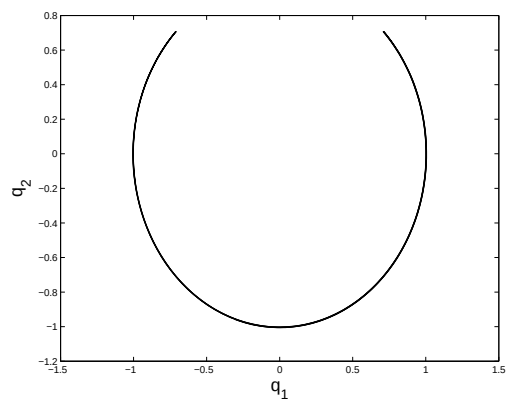

(f) configuration

Figure 1.3: Phase and Configuration Plots: System (1.8) with renormalization (column 1) and the equivalent system (1.12) (column 2).

Column 2 of figure 1.3 illustrates the benefit of this slight of hand. In accord with the explanation for the numerical drift, the elimination of the Lagrange multiplier by algebraic means eradicates this effect. Of course, numerical error will still persist and thus ultimately, it may still be necessary to integrate renormalization into the scheme. However, in this case we would not require it as often and in some sense its employment is closer to justified.

1.5 Control

In this section we take up the issue of control design. We wish to accomplish two objectives in the course of our discussion here. Firstly, we desire to emphasize a central control design philosophy. Secondly, we hope to indicate that once such a framework is decided upon, the coordinates selected to cover the configuration manifold of our system is an auxiliary task and is not central to the design philosophy apart from easing its realization.

The control dogma that we take up is that of feedback linearization. The essence of this tenet is to feedforward inertial forces while employing state feedback to obtain the desired control task of stabilization of state error. While some eschew this practice on the grounds that it is an attempt to avoid the problems presented by non-linear dynamics, we embrace it on the grounds that it is quite natural to do so. In fact, this simple and powerful idea embodies what we quite naturally do on a day to day basis. Indeed, if we enter a curve in the road, do we not lean into it? What is the point of making an object aerodynamic?

For a fully actuated Lagrangian system the process of feedback linearization can be mathematically captured quite succinctly. As previously stated, within a coordinate chart (U, φ) on the system's configuration manifold Q the dynamics of such a system may be written

$$M(\mathbf{q})\ddot{\mathbf{q}} + C(\mathbf{q}, \dot{\mathbf{q}})\dot{\mathbf{q}} + V(\mathbf{q}) = \boldsymbol{\tau} \ , \tag{1.13}$$

where, being more specific at this juncture,

$$\begin{aligned} M_{ij} &= \frac{\partial^2 L}{\partial \dot{q}_i \partial \dot{q}_j} \ , \\ C_{ij} &= \sum_{k=1} \frac{1}{2} \left(\frac{\partial M_{ij}}{\partial q_k} + \frac{\partial M_{ik}}{\partial q_j} - \frac{\partial M_{kj}}{\partial q_i} \right) \dot{q}_k \ , \\ V_i &= \frac{\partial U}{\partial q_i} \ , \end{aligned}$$

and $\boldsymbol{\tau}$ is the vector of impressed forces, i.e. controls, acting along the coordinate directions. One obtains the feedback linearization by feeding forward inertial forces and compensating the potential. That is, we take

$$\tau = M(\mathbf{q})\mathbf{u} + C(\mathbf{q}, \dot{\mathbf{q}})\dot{\mathbf{q}} + V(\mathbf{q}) \ , \tag{1.14}$$

where the vector $\mathbf{u}$ is introduced to permit feedback acceleration control. Closing the loop we obtain

$$\ddot{\mathbf{q}} = \mathbf{u} \ , \tag{1.15}$$

or Newton's equation. Thus the system is rendered in completely reachable linear system form and we may employ any of the linear control techniques in the design of $\mathbf{u}$.

In a very real sense, there is but a single natural linear controller, the PD (Proportional Derivative) controller. Let $\mathbf{q}_d$ denote the desired state of the system and let $\mathbf{e} = \mathbf{q} - \mathbf{q}_d$ denote the existing state of the error. Then the PD controller for trajectory tracking, or error stability, is given by $\mathbf{u} = \ddot{\mathbf{q}}_d - K_v\dot{\mathbf{e}} - K_p\mathbf{e}$, where K_v , $K_p > 0$ are selected to be symmetric. This selection of $\mathbf{u}$ provides the error dynamics:

$$\ddot{\mathbf{e}} + K_v\dot{\mathbf{e}} + K_p\mathbf{e} = 0 \ . \tag{1.16}$$

One should recognize this as the multi-dimensional analogue of the damped oscillator. Indeed, this is an alternate interpretation of the control philosophy we are applying here. The idea is to impress a system of forces which result in a closed loop system whose dynamics take on the character of a well-known system

which has the stability properties desired. The damped oscillator is a well known system whose stability properties for various values of K_p and K_v are well understood, being taught in most elementary courses on the subject of differential equations. In particular, by choosing K_p and K_v to be s.p.d. we have ensured asymptotic *coordinate* trajectory tracking[8].

We illustrate the procedure by applying it to the pendulum system. It is assumed that a bidirectional torque τ may be applied to this mechanism. Thus we have the equation of motion

$$mr^2\ddot{\theta} - mgr\sin(\theta) = -\tau. \tag{1.17}$$

We select

$$\tau = -mr^2 u + mgr\sin(\theta) \ , \tag{1.18a}$$

$$u = \ddot{\theta}_d - K_v\dot{e} - K_p e \ , \tag{1.18b}$$

where $e = \theta - \theta_d$ and K_v , $K_p > 0$ are design parameters left to our choosing. With these choices we of course obtain

$$\ddot{e} + K_v \cdot \dot{e} + K_p \cdot e = 0 \ ,$$

as desired. Now, let us fix an instance of the model by fixing its parameters to $m = r = 1$ once again and suppose that our directive is to stabilize this pendulum's unstable upright equilibria (i.e., $\theta_d = 0$). Setting $K_v = K_p = 1$ we obtain the results of figure 1.4.

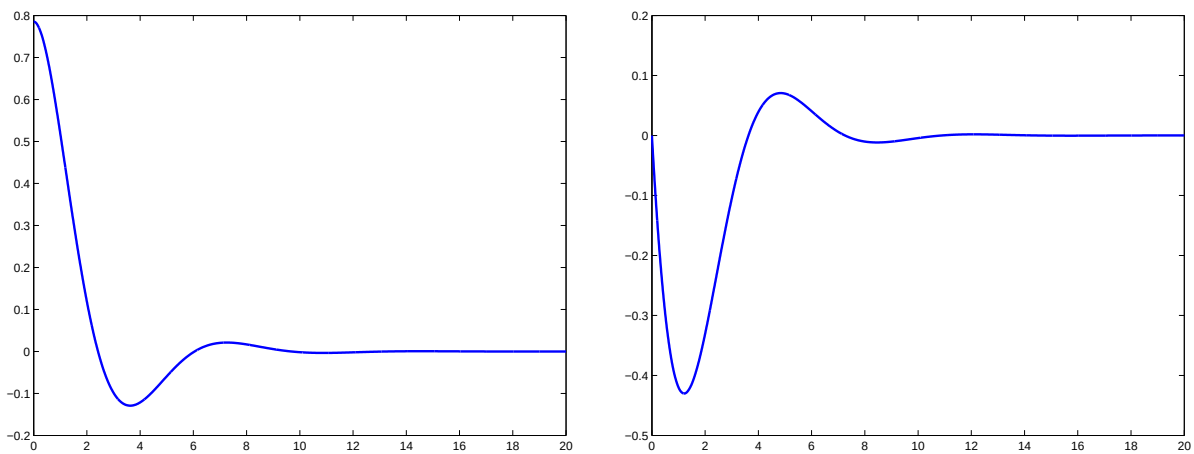

(a) t-θ (b) t-$\dot{\theta}$

Figure 1.4: Feedback linearization control results corresponding to (1.1). Here we've stabilized the pendulum to its upright position $\theta = 0$.

Consider at this juncture the same scenario or task in the context of the overdetermined Cartesian parameterization of S^1. If we take up (1.8) then the control torque τ enters into the system in the following manner

$$\dot{q}_1 = v_1 \ , \tag{1.19a}$$

$$\dot{q}_2 = v_2 \ , \tag{1.19b}$$

$$\dot{v}_1 = -\frac{1}{q_1^2 + q_2^2}\left(v_1^2 + v_2^2 - \frac{mgrq_2}{mr^2}\right)q_1 - \frac{1}{mr^2}\tau q_2 \ , \tag{1.19c}$$

$$\dot{v}_2 = -\frac{1}{q_1^2 + q_2^2}\left(v_1^2 + v_2^2 - \frac{mgrq_2}{mr^2}\right)q_2 - \frac{g}{r} + \frac{1}{mr^2}\tau q_1 \ . \tag{1.19d}$$

i.e., $\boldsymbol{\tau} = \tau(-q_2, q_1)$.

[8]This should not be confused with asymptotic configuration tracking or stabilization.

One could entertain themselves for some time trying to determine how to select τ in this context. To lighten the mood we may work with system (1.12) ($m = r = 1$) in lieu of (1.8) or (1.9). In this case we have the momentum equation

$$\dot{p} = gq_1 - \tau \ . \tag{1.20}$$

Hence the feedback linearization portion of the design is again simple, being $\tau = gq_1 - u$. The quandary here lies with the appropriate determination of an expression for u. For here we reconstruct the cartesian coordinates (q_1, q_2) from their respective derivatives as opposed to θ by means of $\dot{\theta}$. That is, recall the kinematic differential equation

$$v_1 = pq_2 \ ,$$

$$v_2 = -pq_1 \ .$$

Indeed it is possible to design in this context. For instance, see [2]. However, the most direct route in this instance is to design in the context of system (1.1), determining τ as in (1.18), and then evoking immersion relations 1.2 to ascertain $\theta(q_1, q_2)$. Doing so leads to the controller expression

$$\tau = -mr^2 u + mgrq_1 \ , \tag{1.22a}$$

$$u = -K_v(\dot{q}_1 q_2 - q_1 \dot{q}_2) - K_p \tan^{-1}\left(\frac{q_1}{q_2}\right) \ . \tag{1.22b}$$

A subtle point often lost is that we have no need of examining the closed loop properties of systems (1.8) or (1.12) under (1.22) (though one should pay close attention to the extent of validity of coordinate transformations and multiple representations[9]). For stability is a *system property*. If an impressed force promotes a system to a given configuration, then such is so no matter how we care to describe the circumstances. (1.18) and (1.22) are simply two of infinitely many expressions of the force dictated by the control philosophy, which cares not for coordinates. The foretold results of applying (1.22) to system (1.8) are provided in figure 1.5.

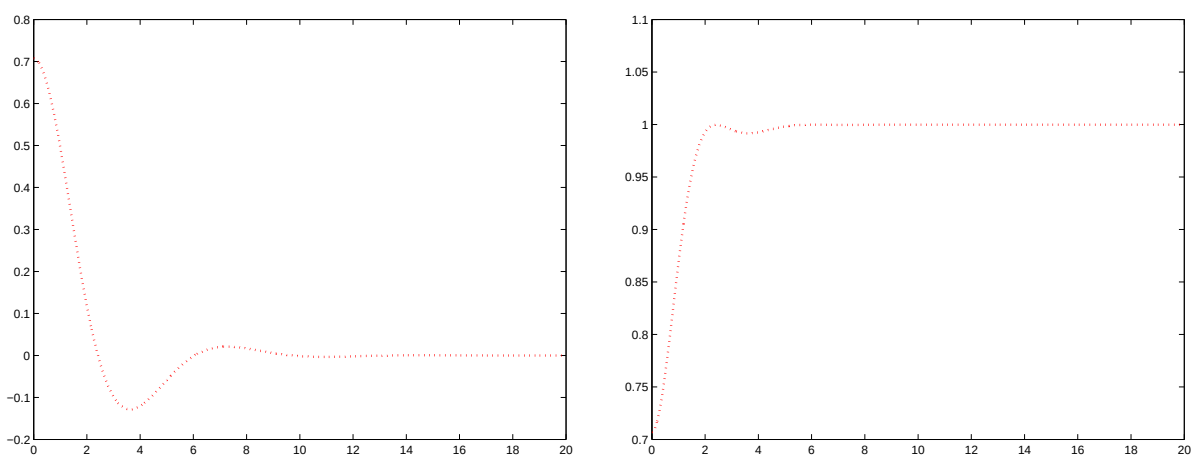

(a) t-q_1 (b) t-q_2

Figure 1.5: Feedback linearization control results corresponding to (1.8). Here we've again stabilized the pendulum to its upright position $(q_1, q_2) = (0, 1)$.

[9]These concerns are symptomatic of the general ills of using coordinate based approaches

1.6 Conclusions and Future Directions

Herein we have drawn upon a system (the simple inverted pendulum) on S^1 in order to establish an inroad to inference regarding modeling and controls design for systems which evolve, or have a component which evolves on, SO_3. Such a jump is possible, being it the case that SO_3 may be identified with S^3. Our desire was to consider the issues which arise upon embedding S^1 into a copy of E^2 parameterized by Cartesian coordinate functions.

One immediate consequence of this embedding was the need to employ the Langrange multiplier in order to account for constraint forces. The issue of how one treats the eventual elimination of this multiplier, should this be the route taken, is naturally induced. What we found is that the typical approach of reducing the index-2 DAE to an index-0 ODE by means of successive differentiation of the constraint equation leads to numerical instability problems. Indeed, we determined by means of relevant literature that this issue is of long standing and is quite general, applying to systems outside of our example.

The resolution of this issue stands as one of the accomplishments generated by this work. It was determined that the multipliers introduced could in fact be eliminated by algebraic means in the problem instance we considered, thus eradicating the instability generated by the typical approach. This observation generates a future course of work. Namely, to consider the problem in its generality and to address those conditions sufficient for extrapolation of the determined solution.

The second issue that we focused on was control design impediments rooted in the embedding. We determined by means of our example problem that the very simple and commonly employed nonlinear control technique of feedback linearization becomes confounded upon introduction of coordinate dependence. The literature indicates that the overdetermined coordinate setting becomes design compliant should one make use of natural coordination of momentum space (or tangent space). However, we found, at least in the case of the pendulum system, that the most direct route to design was through a chart. The resulting controller could then be used in the whatever coordinate setting one would care to choose by making use of the appropriate coordinate transformations.

From these observations we provided an indicator that it may indeed be possible and perhaps advantageous to obviate the practice of designing around coordinates. A central, coordinate free realization of a control philosophy, such as feedback linearization, would be most profitable to the control design community. Future work should involve moving beyond our simple example and indicators. The concepts discussed and illustrated here need to be realized in the setting of S^3 (i.e. attitude control). This would bring thoughts to bear on actual problems of multibody spacecraft modeling and control design.

Acknowledgements

Gregory Hicks

Zhilin Li

Dmitry Zenkov

Bibliography

[1] Marvin J. Forray, Variational Calculus in Science and Engineering, McGraw-Hill Book Company, New York, 1968.

[2] Atul Kelkar and Suresh Joshi, Control of Nonlinear Multibody Flexible Space Structures, Springer-Verlag Berlin Heidelberg, London, 1996.

[3] Thomas R. Kane, Dynamics, Holt, Rinehart and Winston, Inc., U.S.A., 1968.

[4] Cornelius Lanczos, The Variational Principles of Mechanics, Dover Publications, Inc., New York, 1986.

[5] Barrett O'Neill, Elementary Differential Geometry, Acedemic Press Inc., New York and London, 1966.

[6] Hans Sagan, Introduction to the Calculus of Variations, Dover Publications, Inc., New York, 1969.

[7] Ahmed A. Shabana, Dynamics of Multibody Systems, Cambridge University Press, 1989.

[8] A.M. Bloch, Nonholonomic Mechanics and Control, Interdisciplinary Applied Mathematics, Systems and Control, Springer-Verlag New York, Inc., 2003.

[9] Uri M. Ascher and Linda R. Petzold, Computer Methods for Ordinary Differential Equations and Differential-Algebraic Equations, SIAM, 1998.

Chapter 2

MOBILE SENSING OF AEROSOLIZED CHEMICAL AND BIOLOGICAL AGENTS

Natalie Almond[1], Wandi Ding[2], Xiaochuan Li[3], Xingtao Liu[4], Steven Rusnica[5], Ismael Velzquez-Ramrez[6]

Faculty Consultants:
Emily Lada and Kazafumi Ito

Problem Presenter:
Michael C. Horton and Melissa Choi
Massachusetts Institute of Technology, Lincoln Laboratory

Abstract

In the wake of the September 11, 2001 attacks on the United States, homeland defense, including protection against biological and chemical attack, has become an important area of research for the nation. To address this difficult problem, researchers at MIT Lincoln Laboratory are developing sensors to detect the presence of chemical and biological agents in the air. In the event of a chemical or biological attack on a heavily populated area, a network of these detectors could alert officials quickly, minimizing casualties, public panic, and strain on the health care system. Lincoln Laboratory is investigating various architectures for such a detector network. Since the detectors are typically expensive to deploy and operate, it is important to minimize the number of sensors while maintaining the network's overall system detection capability. It has been suggested that placing the detectors on mobile platforms might allow the detection of a bioaerosol plume with fewer detectors than a fixed detector network. The idea here is that the probability of a moving sensor intersecting the path of a moving (due to wind) and dispersing (due to turbulence) bioaerosol plume is much higher than that of a stationary detector. Depending on the conditions of bioaerosol plume release and propagation, detector density, detector platform speed, etc, either the mobile or the fixed detector network would be preferred. We would like to quantitatively assess the number of mobile detectors or fixed detectors required in a network to detect bioaerosol plumes as a function of the driving parameters (plume dispersion modes and rates, wind speed, sensor speed, etc...). We found that although the probability of successful detection by movings sensors

[1]Western Carolina University
[2]University of Tennessee
[3]University of S. Mississippi
[4]SUNY
[5]Allegheny College/NCSU
[6]Universidad Autónoma Metropolitana, Iztapalapa

is slightly higher than that of fixed sensors, the cost of installing moving sensors will outweigh the benefits. We therefore recommend using fixed sensors.

2.1 Introduction and Motivation

Biological or chemical attacks in the United States have been a very important topic, not only because of the real problem which was founded at the September 11, 2001 attacks, but also because of the multiple ideas that researchers have proposed. A good example of this is the construction of sensors to detect the presence of chemical and biological agents in the air made by MIT Lincoln Laboratory, which was funded by the United States Department of Defense. Due to the expensive manufacturing cost of each sensor we must minimize the number of sensors and allocate them in the quickest way to detect the bioaerosol plume. It has been suggested that placing the detectors on mobile platforms might allow the detection of a bioaerosol plume with fewer detectors than that of a fixed detector network. Our main goal is analyzing mathematically the two networks in order to simulate, compare, and find the best way to allocate the sensors and determine which network is more effective.

The best way to approach the problem is to describe an attack. There are several release scenarios for an attack, they are as follows. 1. Point-burst, 2. Point-sustained, 3.Line (sustained), 4. Curve (sustained), 5. Point-burst, Intermittent, 6. etc...; we will focus on the first two.

We will use the Gaussian Plume Models in order to describe these kinds of attacks. These models have been built using Fickian diffusion and were introduced in 1932 by O.G. Sutton (see Sutton [3]), and in 1981 by Bianconi (see Bianconi [2]) respectively.

Following Sutton, the chemical concentration in the point-burst release will be

$$C(x,y,z,t) = \frac{M_A}{(2\pi)^{3/2}\sigma_y^2\sigma_z}\left\{\exp\left[-\frac{(z-z_s)^2}{2\sigma_z^2}\right] + \exp\left[-\frac{(z+z_s)^2}{2\sigma_z^2}\right]\right\}\cdot \exp\left[-\frac{(x-x_s-u_x(t-t_0))^2+(y-y_s-u_y(t-t_0))^2}{2\sigma_y^2}\right] \tag{2.1.1}$$

where

M_A	Release mass
(x_s, y_s, z_s, t_0)	Release Point
u	Wind Velocity
$u_x = u\cos\theta$	Wind Velocity Components
$u_y = u\sin\theta$	
θ	Downwind Direction
$(\sigma_x, \sigma_y, \sigma_z)$	Plume Spread.

For our model the mobile or fixed sensors can be at the same height, so we can expect the variable z =cte will be a good observation plane. If we choose the origin such that $z = 0$ this will be the sensors height and we suppose that $z_s = 0$, it follows

$$\bar{C}(x,y,t) = \frac{2M_A}{(2\pi)^{3/2}\sigma_y^2\sigma_z}\exp\left[-\frac{(x-x_s-u_x(t-t_0))^2+(y-y_s-u_y(t-t_0))^2}{2\sigma_y^2}\right] \tag{2.1.2}$$

that is the projection of the equation 2.1.1 into the plane $z = 0$.

The plume spreads, σ's will be parameterized with respect to the downwind distance using the Pasquilli-Gifford parameters $\{c_y, e_y, c_z, e_z\}$ (see Turner [1])

$$\left.\begin{aligned}\sigma_y(\bar{x}) &= c_y|d_{DW}(\bar{x})|^{e_y}\\ \sigma_z(\bar{x}) &= c_z|d_{DW}(\bar{x})|^{e_z}\end{aligned}\right\} \tag{2.1.3}$$

where the downwind distance is

$$d_{DW}(x,y) = (x-x_s)\cos\theta + (y-y_s)\sin\theta. \tag{2.1.4}$$

Model	c_y	e_y	c_z	e_z
a-Very Unstable	0.18	0.92	0.72	0.76
b-Moderately Unstable	0.14	0.92	0.53	0.73
c-Slightly Unstable	0.1	0.92	0.34	0.72
d-Neutral	0.06	0.92	0.15	0.7
e-Slightly Stable	0.045	0.91	0.12	0.67
f-Very Stable	0.03	0.9	0.08	0.64

Table 2.1.1: Quasi-Instantaneous Power Function.

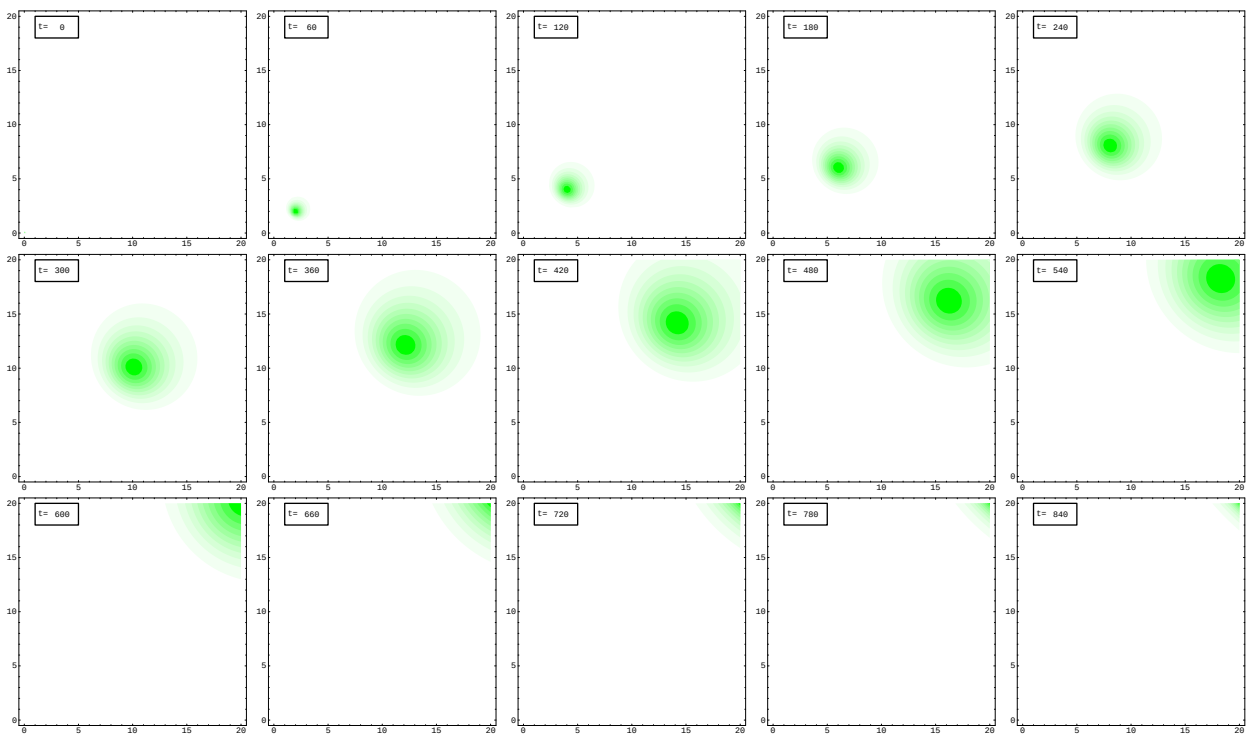

Figure 2.1.1: Simulating the chemical concentration in the point-burst release with $M_a = 100$, $(x_s, y_s) = (.01km, .01km)$, $u = .05km/s$, $\theta = \pi/4$.

Pasquilli and Gifford have divided the air conditions into six stability classes (see Turner [1]), and when the σ's are parasitized as in 2.1.3, we can choose the Pasquilli-Gifford parameter according to the following table

Now, following Bianconi, the chemical concentration in the point-sustained release will be

$$C(x,y,z,t) = \frac{M_A}{4\pi\sigma_y\sigma_z u T_A}\left\{\exp\left[-\frac{(z-z_s)^2}{2\sigma_z^2}\right] + \exp\left[-\frac{(z+z_s)^2}{2\sigma_z^2}\right]\right\}\cdot$$
$$e^{-\frac{d_{CW}^2}{2\sigma_y^2}}\left[\operatorname{erf}(kt-b) - \operatorname{erf}(k(t-T_A)h(t-T_A)-b)\right] \quad (2.1.5)$$

where

T_A		Duration of exposure
$k =$	$\frac{u}{\sqrt{2}\sigma_y}$	
$b =$	$\frac{d_{DW}}{\sqrt{2}\sigma_y}$	
$d_x =$	$(x-x_s)\sin\theta - (y-y_s)\cos\theta$	Crosswind distance
$h(t-T_A) =$	$\begin{cases} 0, & t < T_A \\ 1, & t \geq T_a \end{cases}$	Heaviside step function.

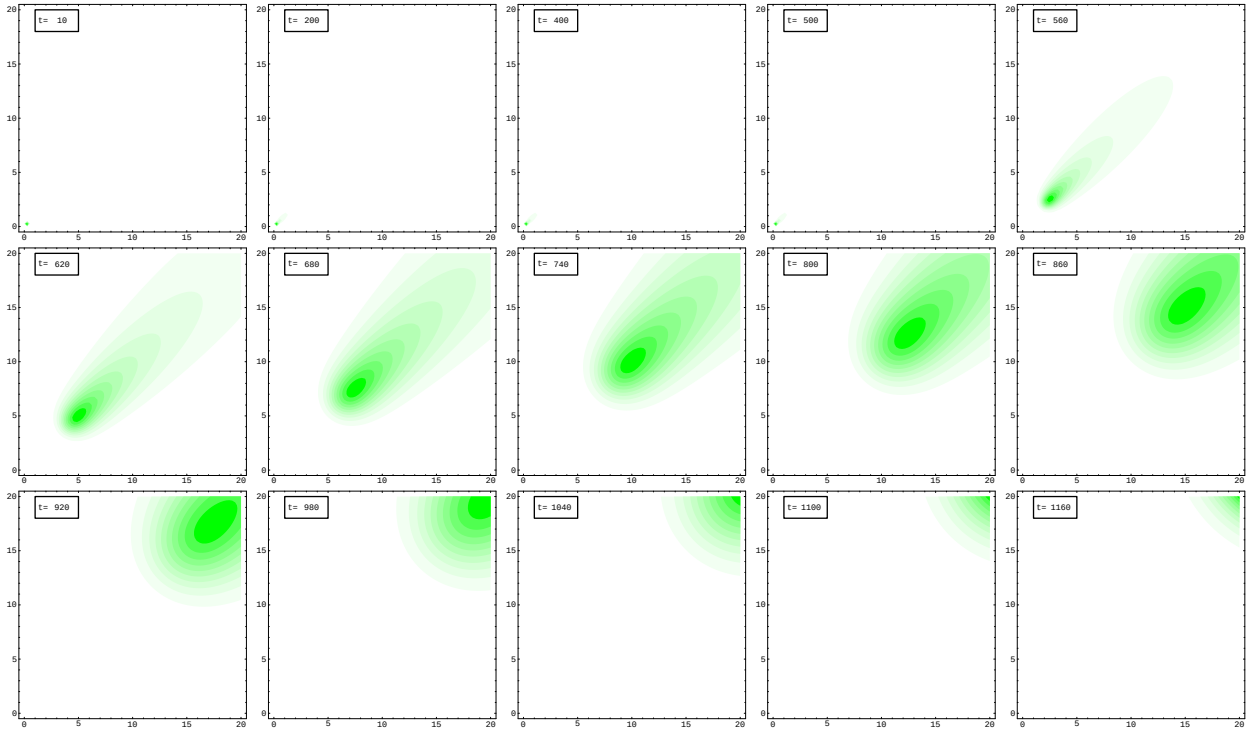

Figure 2.1.2: Simulating the chemical concentration in the point-sustained release with $M_a = 100$, $(x_s, y_s) = (.01km, .01km)$, $u = .05km/s$, $\theta = \pi/4$, $T_A = 500$s.

At this point we just have a plume description, our goal now is to determine the probability of detecting the plume by some time t when we are using k sensors, either stationary or moving at some fixed speed.

After running instantaneous point-release simulations to observe the behavior of the plume, we noticed that at any given time the shape of the plume resembles a disk (see Figure 2.1.1).

We let each moving sensor be represented by a needle of length l, where the needle represents the path of the moving sensor, we are going to assume that the speed of the moving sensors is much higher than that of the spread of the plume. Since we are placing the moving sensors randomly throughout a 20 km $\times$ 20 km observation area, the probability of a moving sensor detecting the plume is the same as the probability that at least one point of the needle is within the circle which represents the area of the plume. In order to use this model, we need to know several things. First, we want to know the radius of the circle in terms of t. Second, what is the probability that a point of the needle is within the circle, when the needle is dropped randomly in the observation area? Third, we need to determine a reasonable needle length l. Finally, we want to know what is the probability that the plume was detected by some time t. We have an underlying problem, we need to determine the time in which the plumes size changes minimally.

2.2 Estimating Area

We have observed that the simulating of the plume in the point burst release spread looks like circles at any time, according with the introduction part we shall use this fact strongly, for that reason we need to give enough arguments in order to use this fact.

Let $\bar{C}_m$ the minimum concentration which can be detected by a sensor. Then by 2.1.2, we obtain

$$(x - x_s - u_x(t - t_0))^2 + (y - y_s - u_y(t - t_0))^2 = 2\sigma_y^2 \ln\left(\frac{2M_A}{(2\pi)^{3/2}\sigma_y^2\sigma_z\bar{C}_m}\right) \tag{2.2.1}$$

the level curve when $\bar{C}(x, y, t) = \bar{C}_m$. Each point from the level curve (x, y) depend on the time and we can

see them as particles moving from the release point by the air affect, for that reason, the assumption

$$d_{DW} \approx ut,$$

downwind distance is similar to the distance of a particle in the curve level which travel from the release point in the downwind direction at constant velocity u, is acceptable. Using this fact in the equation 2.2.1 we have

$$(x - x_s - u_x(t - t_0))^2 + (y - y_s - u_y(t - t_0))^2 = 2C_y^2(ut)^{2e_y}[\ln A - 2(e_y + e_z)\ln(ut)]. \tag{2.2.2}$$

where $A = \frac{2M_A}{(2\pi)^{3/2}\bar{C}_m}$. We can easily note that 2.2.1 is a circle with center in $\big(x_s + u_x(t - t_0))^2, y_s + u_y(t - t_0)\big)$ and radius

$$r = 2C_y^2(ut)^{2e_y}[\ln A - 2(e_y + e_z)\ln(ut)] \tag{2.2.3}$$

using this result, we are able to approximate the radius of the disk where the plume is within detectable range as a function of t.

2.3 Probability of a Needle Intersecting a Circle

In this part we will build a simular construction made by H. J. Khamis [4]. To compute the probability that a randomly dropped needle of length l crosses a circle of radius r contained in the observation area of 20 km $\times$ 20 km, we will refer to the area as a board. Let C be the event that the needle crosses the circle with radius r. First, we divide the problem into two events

- I_1 the event that the midpoint of the needle falls inside the circle of radius r.
- I_2 the event that the midpoint of the needle falls inside the observation area but outside the circle of radius r.

Given the event I_1, the probability of a cross is one. Therefore, we will focus on computing the probability of a cross given the event I_2. Let X be the distance between the midpoint (M) of the needle and the circumference, as measured along the radius extending from the center (0) through the midpoint of the needle. Let Θ represent the acute angle created by $0M$ and the needle. Let s be the distance from 0 to the endpoint of the needle E (see the Figure 2.3.1).

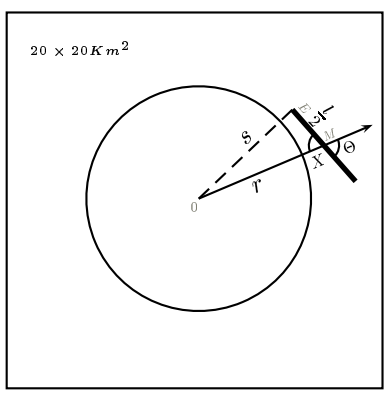

Figure 2.3.1: A needle of length l dropped randomly in an observation area of 20 km $\times$ 20 km, which contains a circle of radius r.

Using the Law of Cosines, we have

$$\begin{aligned} s^2 &= (r + x)^2 + \left(\frac{l}{2}\right)^2 - 2(r + x)\frac{l}{2}\cos\theta \\ &= (r + x)^2 + \frac{l}{4} - (r + x)l\cos\theta. \end{aligned}$$

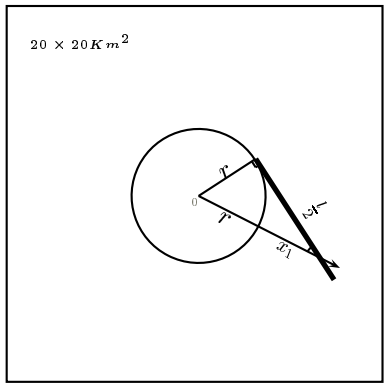

Figure 2.3.2: Case when the left end point of the needle E coincides with the point at which the needle is tangent to the circle.

Now, if we let x_1 represent the value of x when the left end point of the needle E coincides with the point at which the needle is tangent to the circle having radius r (see Figure 2.3.2), then we have

$$x_1 = \frac{1}{2}\sqrt{l^2 + 4r^2} - r.$$

We will now compute the probability density function (pdf) of X. The probability that M falls in the box at a distance between 0 and x from the circle with radius r, denoted by $F_X(x)$, is the ratio of the area of the annulus having radius r and outer radius $(r + x)$ to the area of the box of dimension $20 \times 20\text{km}^2$, excluding the area of the circle of radius r

$$F_X(x) = \frac{\pi(r+x)^2 - \pi r^2}{400 - \pi r^2} = \frac{x^2 + 2rx}{\frac{400}{\pi} - r^2}.$$

Then we have the following formula for the pdf of X:

$$f_X(x) = \frac{d}{dx}F_X(x) = \frac{2(x+r)}{\frac{400}{\pi} - r^2}.$$

Note that $0 < x < D$, where D is the minimum distance between the circle and the box. All computations are made with the assumption that D is not zero and $D \geq l$, implying $r > 10 - l$ and $r > 0$.

The next step is to divide the problem into the following three cases:

- $0 < X < x_1$.
- $x_1 < X < l/2$.
- $X > l/2$.

In the third case, the probability that the needle touches the circle is zero, so we will just check the first two cases (see the Figure 2.3.3).

(a) Case 1: $0 < X < x_1$

In this case, the needle crosses the circle with radius r if and only if

$$s^2 < r^2 + \left[\frac{l}{2} - \sqrt{(r+x)^2 - r^2}\right]^2,$$

where the right hand side of the above equation is the value of s^2 when the needle is tangent. This implies

$$\cos\theta < \frac{\sqrt{(r+x)^2 - r^2}}{r+x}.$$

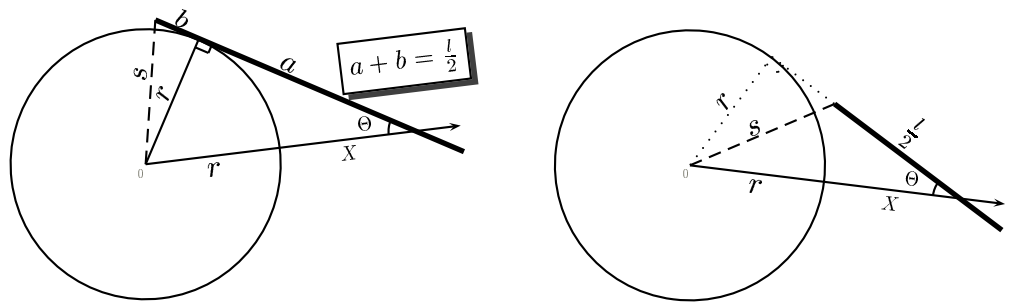

(a) $0 < X < x_1$ (b) $x_1 < X < l/2$

Figure 2.3.3: The two posible cases for X.

So that

$$\theta < \cos^{-1}\left[\sqrt{1-\frac{r^2}{(r+x)^2}}\right] = Z.$$

Now, since θ is uniform on $[0, \pi/2]$, we have

$$P(\theta < Z) = \int_0^Z \frac{2}{\pi} d\theta = \frac{2}{\pi} Z.$$

The joint probability of a success C on the circle of radius r for the case $0 < x < x_1$ given event I_2 is

$$\begin{aligned} &P(C, 0 < X < x_1 | I_2) = \\ &= \left(\frac{2}{\pi}\right) \frac{2}{\frac{400}{\pi} - r^2} \int_0^{x_1} (x+r) cos^{-1}\left(\sqrt{1-\frac{r^2}{(r+x)^2}}\right) dx \\ &= \frac{1}{400-\pi r^2}\left(\frac{4r^2+l^2}{2} cos^{-1}\left(\frac{l}{\sqrt{4r^2+l^2}}\right) + r(l-\pi r)\right). \end{aligned}$$

(b) Case 2: $x_1 < X < l/2$

In this case, the needle crosses the circle with radius r if and only if $s < r$. Or if

$$\theta < \cos^{-1}\left[\frac{(x+r)^2 + \frac{l^2}{4} - r^2}{(r+x)l}\right] = Q.$$

Since θ is uniform on $[0, \pi/2]$, we have $p(\theta < Q) = \frac{2}{\pi} Q$.

The joint probability of a crossing C for the case $x_1 < x < l/2, \theta < Q$ given event I_2, since X and θ are independent, is:

$$\begin{aligned} &P(C, x_1 < X < l/2 | I_2) = \\ &\frac{4}{400-\pi r^2} \int_{x_1}^{l/2} (x+r) cos^{-1}\left(\frac{(x+r)^2 + (l^2/4 - r^2)}{(x+r)l}\right) dx = . \\ &\frac{1}{400-\pi r^2}\left(r(l+\pi r) - \frac{4r^2+l^2}{2} cos^{-1}\left(\frac{l}{\sqrt{4r^2+l^2}}\right)\right) \end{aligned}$$

Then if we combine these two joint probabilities, we have $P(C|I_2) = \frac{2lr}{400-\pi r^2}$.

Finally we have

$$\begin{aligned} P(C) &= P(C|I_1)P(I_1) + P(C|I_2)P(I_2) \\ &= (1)\left(\frac{\pi r^2}{400}\right) + \frac{2lr}{400-\pi r^2}\left(\frac{400-\pi r^2}{400}\right) \\ &= \frac{2lr}{400} + \frac{\pi r^2}{400}. \end{aligned} \tag{2.3.1}$$

2.4 Probability of Detection by a Given Time

Now that we have the area as a function of t and the probability of a needle intersecting a circle of a given radius, we can compute the probability of detecting the plume by some time t, therefore we have the probability that at least one point of the needle will fall within the circle when we drop the needle randomly on the board. It is as follows:
$P(C_t)$ = Probability that at least one point of a needle is with in the circle.
$R(t)$ = Radius of the plume disk that is within detectable range at time t.
$P(t)$ = Probability that a plume is detected by some time t.

Where

$$P(C_t) = \frac{\pi R(t)^2 + 2lR(t)}{400},$$

$$R(t) = (2C_y^2(ut)^{2e_y}[\ln A - 2(e_y + e_z)\ln(ut))^{1/2}.$$

Assume that $P(t)$ is independent for $t = t_0, t_1, t_2, ..., t_k$ Then

$$\begin{aligned} P(t) &= \sum_{i=1}^{k}\prod_{j=1}^{i}(1 - P(C_{t_{i-1}}))P(C_{t_i}) \\ &= 1 - \prod_{i=1}^{k}(1 - P(C_{t_i})) \end{aligned}$$

where $t = t_k$ and $P(C_{t_0}) = 0$

Now since we assumed independence, we are assuming that the intersection of the disks of the plume at t_j and t_{j+1} is zero. We did not compute the probability using strict independence, however. What we did do to find the t_j's was to find the interval needed to ensure that the disk at t_{j+1} contained at most 10% of the disk at t_j. Since the interval varied, we also needed to use different needle lengths for each interval. The needle length is based on the distance that a moving sensor would cover a certain area, traveling at a fixed speed on that interval. That is, $l_i = V(t_i - t_{i-1})$, where V is the velocity of the moving sensor.

2.5 Simulation

The simulations are divided among three parts. The first part, has been showed through the paper, it is the simulation of the attack. See figures 2.1.1 and 2.1.2 which show snapshots of the moving plume.

The second part, is related to the checking the differences between the real plume and the plume expressed by the circles with fixed radius at each time t. We are using the formula 2.2.3. The way that we are found the real formula is dividing the 20×20 board into equal space grids, say 1001x1001(NxN) (If we refine the grid points, we will get better approximation), also define a mark matrix M. for each grid point, if concentration at this point is equal to or greater than 5e-7(this number was obtained from 25 ACPLA), then at corresponding position of M, we mark it as 1's, else 0. After running through all the grid points, we count the number of 1 in matrix M, then times $(20000/(N-1))^2$, then we get a approximating area. In the figure 2.5.1 we show the tendency of the real problem compared with the approximation.

Finally, in the third part, we show our main result the graphical comparison between the detection of the fixed sensor and mobile sensor, we preset two different velocities in the mobile sensors, supposing that it is traveling in a bus, 36km/h and 72km/h (see the figure 2.5.1)

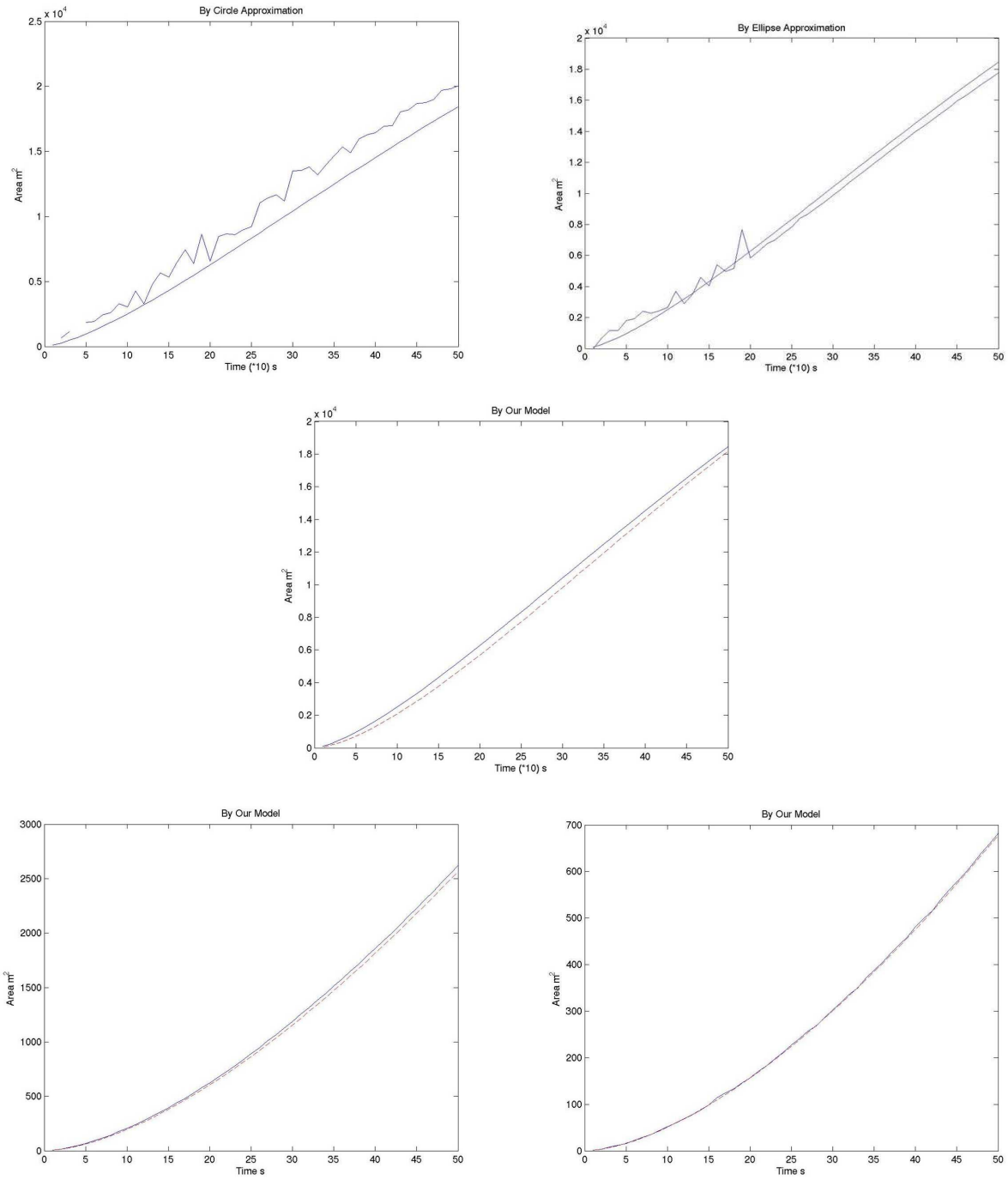

Figure 2.5.1: Differences between the circle model and the real model

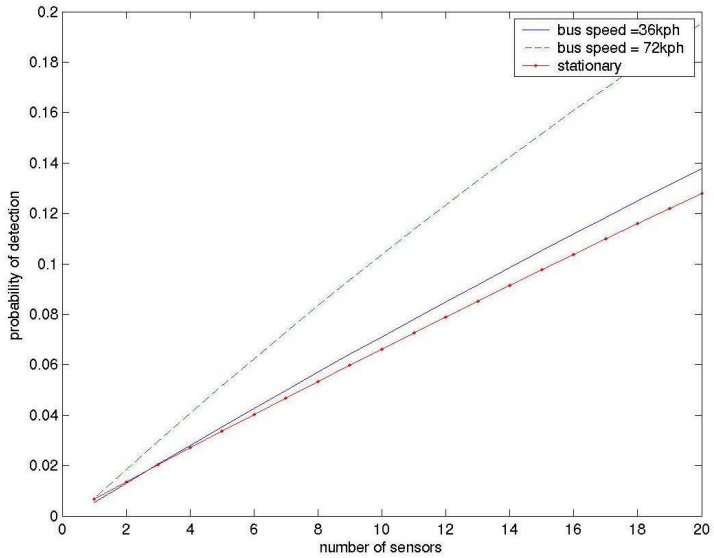

Figure 2.5.2: Simulating mobile sensor with different bus speeds and fix sensors.

2.6 Conclusions

Before we establish the main conclusion based on the discussions in the previous sections, we first want to summarize the independent results in the work.

- The plume in the context of atmospheric dispersion , can be simulated as a circles under stable condition according with the Pasquilli-Guiford scale. (See figures 2.1.1 and 2.5.1)
- Although in the case of point sustained release does not look as a circles (see 2.1.2) the approximation is not too bad (see 2.5.1)
- The difference between the probability of detecting in the plume when the plume radius is r and the needle length is l is determined by
$$\frac{2rl}{400}$$
noted that although this can be a very big amount, when the r is very small this amount is small too.

Now we can interpret the Figure 2.5.2, we can observe the probability of a success with a mobile sensor is slightly higher than that of a fixed sensor, but we need to remember that the bus speed in some cities is too slow. Which can cause for a delayed success for a mobile sensor. It is also evident that the mobile sensors are more expensive to install than the fixed sensors. Since the probability of success with mobile sensors is not significantly higher than the probability of a success with fixed sensors the team's recommendation is to focus more on fixed sensors and find an optimal network that offers the best security against biological or chemical warfare on the United States.

Bibliography

[1] D.B. Turner, *Workbook of Atmospheric Dispersion Estimates An Introduction to Dispersion Modeling*, Lewis Publishers, 1994.

[2] R. Bianconi, *A mathematical model of diffusion from a steady source of short duration in a finite mixing layer* , Atmospheric Environment. Part A. General Topics, vol. 27, number 5, pp. 781-792, April 1993.

[3] Sutton O.G., *A theory of eddy diffusion in the atmosphere*, Proc. Roy. Soc. A, vol. 135, pp 143-165, 1932.

[4] H.J. Khamis, *On Buffon's needle problem using concentric circles*, Pi Mu Epsilon Journal, vol. 8, number 6, pp. 368-376, 1987.

Chapter 3

PROBLEM 3: Optimized Design of Electron Guns for High Power RF Applications

Harshini Fernando[1], Yuan Liu[2], Kui Ren[3], Ivan Rothstein[4], Kelly Sweetingham[5], Tamara Vaughan[6]

Problem Presenter:
Lawrence Ives
Calabazas Creek Research, Inc.

Faculty Consultant:
Hien Tran
North Carolina State University

Abstract

The goal of this project is to provide an analysis, from first principles, for the optimal design of an electron gun. This analysis is subsequently used concurrently with existing optimization code to create and understand the optimal design for an electron gun. The end purpose is the creation of a particle accelerator.

We begin by finding the properties needed for the electron beam to be laminar, since the magnetic field is predetermined and thus can only be adjusted within a given tolerance. For the beam to be laminar, it must have no radial force. Using several laws of physics, we find that, for the outermost electron of the beam ($r = 2.5in$), the angular velocity must equal $4.1 \times 10^6 \frac{m}{s}$.

The next step in the process is to find the optimal shape of the cathode. In order to do this, we first compute the radius of the cathode. Utilizing the conservation of the canonical angular momentum, we can compute the distance between the center line of the cathode and the outermost electron, thus finding that the radius of the cathode is 1.6 in. Using a pre-existing optimization code, we attempt to find the optimal shape for the cathode. Unfortunately, this code was written to optimize the cathode without the presence of a magnetic field. Due to time restraints, we were unable to adequately modify the code to include a magnetic field.

[1]Texas Tech University
[2]University of North Carolina-Wilimington
[3]Columbia University
[4]Virginia Tech
[5]North Carolina State University
[6]University of Alabama-Birmingham

3.1 Introduction and Motivation

High power radio frequency (RF) sources employ electron beams to run the RF circuit. These beams are emitted via an electron gun, which consists primarily of a cathode, anode, focusing element, and a beam tunnel. Calabazas Creek Research, Inc., a nationally recognized company conducting research and design of high powered RF sources, has been hired by Fermi National Laboratory to create a new electron gun for a klystron. Klystrons have multiple applications, ranging from industrial heating to medicine. This particular klystron needs to produce 5 MW of RF power using six electron beams operating at 80,000 V. The gun will utilize a non-convergent electron beam, confined by a constant magnetic field. Reference Figure (1) for a picture of a typical eight beam klystron under construction.

Typically, when designing electron guns, the magnetic field is adjusted to force the electron beam to be laminar. Our aim is to design an electron gun that produces a laminar beam, but with a predetermined magnetic field. The difficulty in this problem is that we must maintain a correct beam current and have a uniform current density profile, while conserving canonical angular momentum and balance between magnetic force and beam space charge forces. In order to do this, we must create the optimal geometric shape for the cathode, which projects the electrons, as well as determine the distance between the anode and cathode to ensure the correct beam current. Conventional cathodes use spherical, constant radii surfaces because the performance can be analytically calculated and they are easily drawn. Unfortunately, this standard shape cannot generate the fields required to create extremely laminar beams.

Our approach to solving this problem is to first examine the beam properties of a laminar field. With this information we will trace the path of several electrons back to the cathode to determine the geometric properties needed to produce this laminar beam. We compare our results with the information provided by an optimization code previously written by B.M. Lewis from North Carolina State University [1].

3.2 A Brief Description of the Electron Gun

The cathode, anode and focusing element collectively determine the performance of the electron gun. The cathode is a negatively charged electrode, while the anode is positively charged. Our cathode uses thermionic emission, rather than secondary emission, to release electrons from its surface. Hence, electron acceleration is generated by the potential energy from the anode region. The electrons are emitted perpendicular to the cathode surface and a focusing element corrects the emission paths at the ends of the cathode, allowing for uniform focusing into the beam tunnel. Otherwise, some of the electrons do not enter the beam tunnel and thus energy is lost. The focusing element extends past the end of the cathode and creates the Pierce angle at approximately thirty seven degrees. Figure 2 shows a diagram of a typical Pierce electron gun, including the Pierce angle.

The magnetic field is created by a solenoid surrounding the beam tunnel. This field balances the space charge forces in the electron beam as it traverses through the RF circuit. Without the magnetic field in place, the electron beam would converge only until it reached its minimum and then would begin to diverge. For this problem, we are using a constant magnetic field for beam confinement.

3.3 Creating a Laminar Beam

In order to find the optimal shape for the cathode, we first determine the electron beam properties in the beam tunnel, given the specifications of this particular klystron. These requirements are:

- Beam Voltage, $V_B = 77$ kV
- Beam Current, $I_B = 22$ Amp
- Beam Radius, $r_B = 2.5$ in

The radius is held at 65% of the wall radius to prevent damage to the tunnel during beam divergence. Figure (3) shows the beam divergence in the absence of a magnetic field. Notice how this divergence causes the electrons to collide with the tunnel wall.

Figure 3.2.1: Electron gun under construction

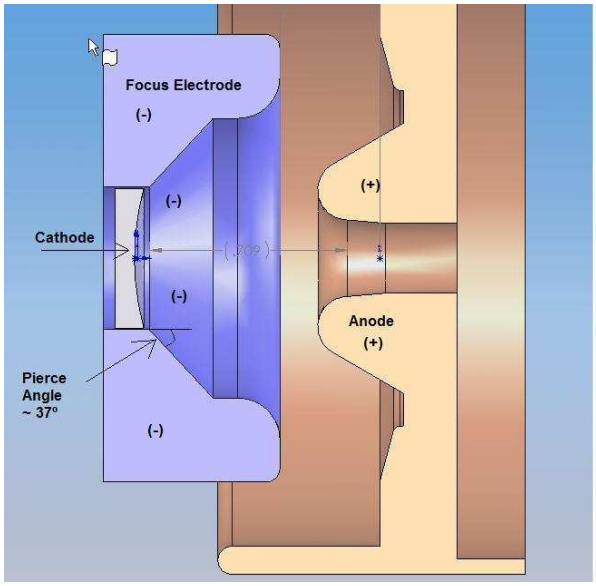

Figure 3.2.2: Cross-section of a Pierce electron gun

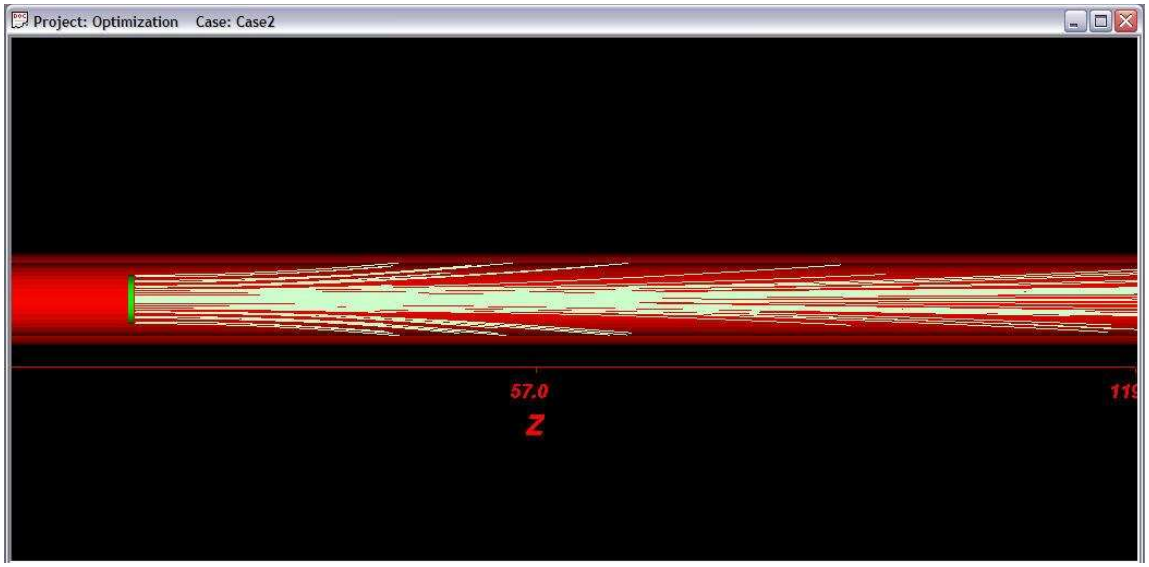

Figure 3.3.1: Divergence of an electron beam without the presence of a magnetic field

In an electromagnetic field, the force is given by

$$F = q(E + V \times B),$$

where E is the electric field and B is magnetic field. Since we desire laminar beam travel, there must be no radial force. Hence we solve,

$$E_r + V_\theta B_z = 0, \tag{3.3.1}$$

with E_r representing the electric field generated by radial motion, V_θ is the angular velocity, and B_z is the existent magnetic field.

From the given data, we can find the Brillouin field using the equation

$$B_B = 0.83 \times 10^{-3} \frac{I_B^{\frac{1}{2}}}{r_B V_B^{\frac{1}{4}}}.$$

The magnetic field, B_Z, is 102 Gauss, since $B_Z = \alpha B_B$. We set $\alpha = 2.5$, usually this varies up to 3.0 for practical reasons. Keeping this quantity low helps to manage cost, while still being able to control the laminar flow of the beam.

Gauss' Law tells us that

$$E_r = \frac{I_B r}{2\pi r_B^2 \epsilon_0 u_0}, \tag{3.3.2}$$

where $\epsilon_0 = 8.854 \times 10^{-12} \frac{\mathrm{F}}{\mathrm{m}}$ and u_0 is obtained using energy conservation $\frac{1}{2} m_0 u_0^2 = m V_B$, which leads to $u_0 = \sqrt{\frac{2eV_B}{m_0}}$ (m_0 is the mass of the electron and e is the charge of the electron). The unknown r is the radius relative to each electron path.

Note that the self-induced magnetic field is given by Ampere's Law

$$\oint H \cdot dl = I,$$

which is a small quantity and thus negligible in our calculations.

Using the radius $r_B = 2.5$, choose eleven values for r, equally distanced with $r_{10} = 2.5$. For each r_i, we find the generated electric field, E_r, and the angular velocity, $V_\theta(r)$, by Equation (2) and solving Equation (1). The corresponding results are represented in Figures (4) and (5), respectively.

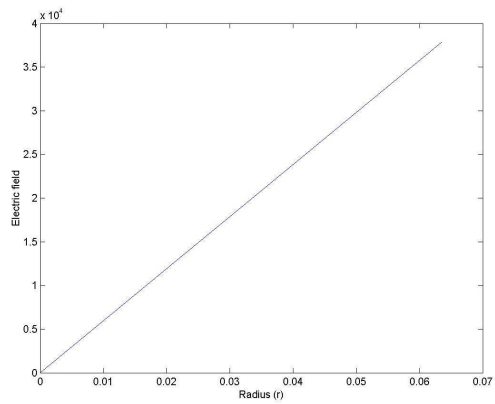

Figure 3.3.2: Electric field (V/m) induced by electron current at different radii (m)

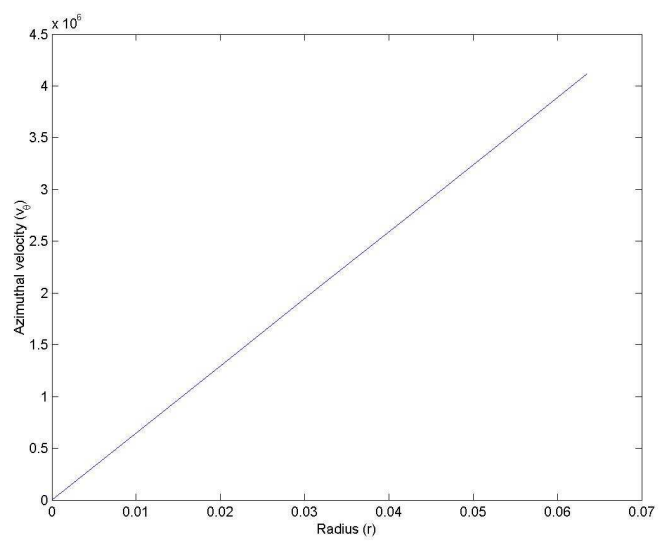

Figure 3.3.3: Azimuthal velocity (m/s) of electrons at different radial positions (m)

By making V_θ a function of r, we know the properties which will produce a laminar beam with a predetermined magnetic field.

(All the pictures in this section were produced using Beam Optics Analysis (BOA), a 3-D particle pusher designed by Calabazas Creek Research, Inc.)

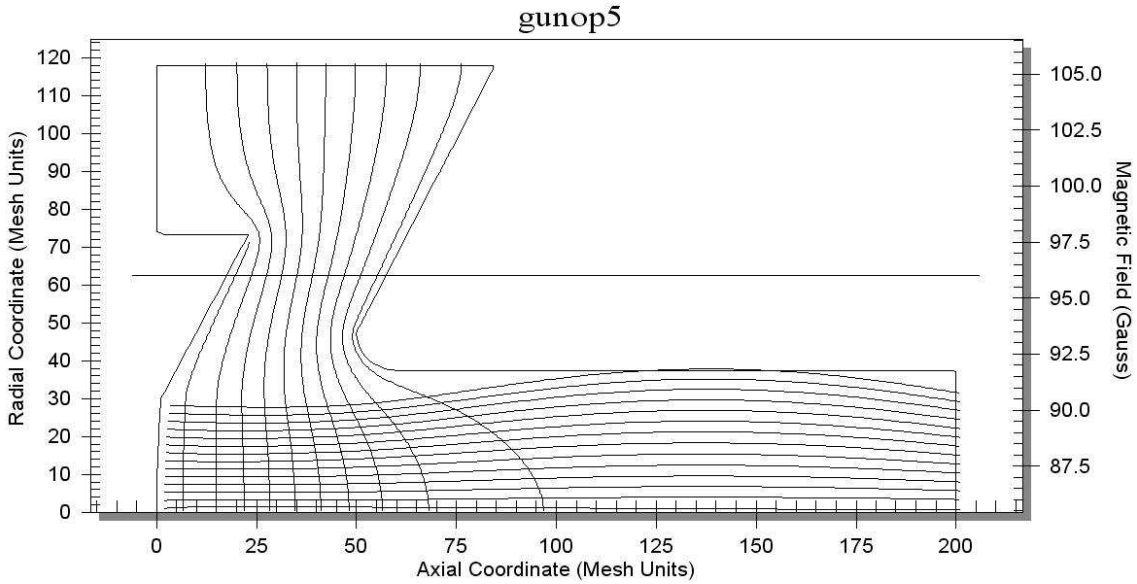

Figure 3.4.1: Simulation of electron gun with $r = 3.4$in

3.4 Finding the Radius of the Cathode

Now that we know the angular velocity required to make a laminar beam, we must determine the geometric shape of the cathode that will produce this beam. We need to find the radius of the outermost electron to the center line of the cathode. We begin by using the fact that the canonical angular momentum of electrons is conserved [2]. The conservation principle is

$$\gamma m_0 r_B V_\theta(r) - \frac{1}{2} e r_B^2 B_Z = -\frac{1}{2} e r^2 B_Z,$$

where the scaling factor, γ, is

$$\frac{1}{\sqrt{1 - \frac{u_0^2}{c^2}}}$$

and the unknown r is the radius to the center line of the cathode at the injection point. This equation reduces to

$$r = \sqrt{r_B^2 - \frac{2\gamma V_\theta(r) m_0 r_B}{e B_Z}}. \tag{3.4.1}$$

Using the angular velocity generated in Figure (5) for the outermost electron, we have $r = 1.6$in. Notice, this value is smaller than the beam radius in the tunnel (2.5 in). Our intuition suggests that the radius of the cathode should be larger than the tunnel radius due to the convergence to the beam minimum. Further investigation leads to changing the sign in Equation (3) since we are tracking beam travel backward to the cathode, thus changing the direction of the velocity. The new radius, r, is 3.4in. Applying this estimation to EGUN, the electron beam rapidly diverges, telling us that our r value was incorrect, as shown in Figure (6). Going back and running the original $r = 1.6$, we do in fact observe a laminar beam. Referring to Figures (7) and (8), we see support for or initial calculation of a smaller cathode radius.

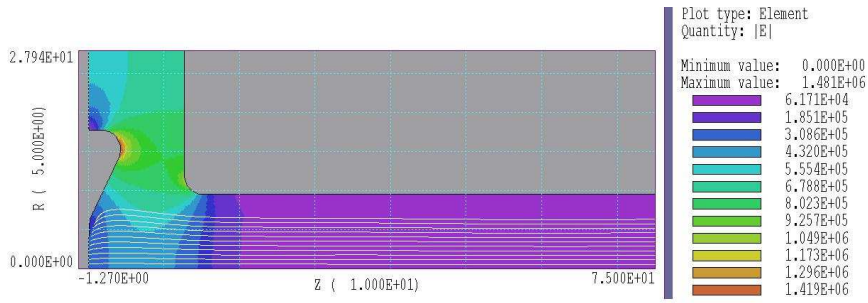

Figure 3.4.2: Laminar beam produced by tracking the electrons backward to the cathode

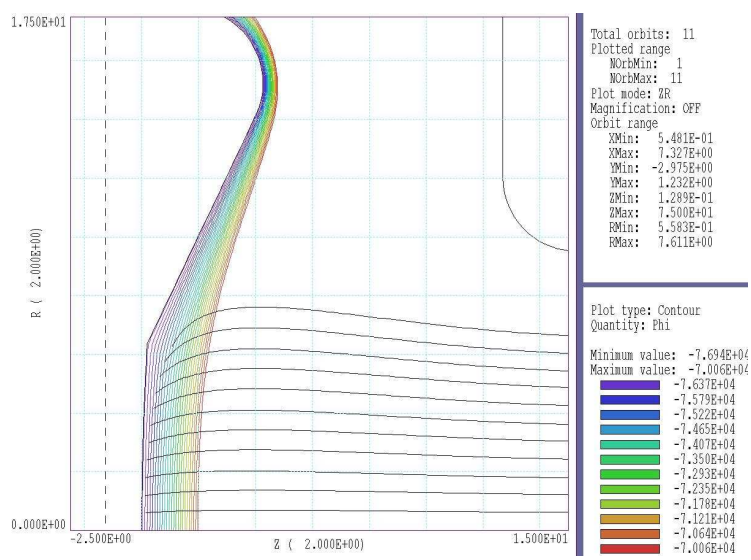

Figure 3.4.3: Close up of cathode region from Figure(7)

3.5 Optimizing the Shape of the Cathode

The optimal design process essentially consists of determining a set of parameters in electron guns such that the output of numerical simulation satisfies our objective mentioned above. The parameters that we change include the following: the shape of the cathode, the distance between the cathode and the anode D_s, the injection position of electrons ,which we denote by R_i and the external magnetic field. The shape of the cathode is parameterized by its radius, denoted by R_c (which slightly different from the spline parameterization used in the previous optimization code by Lewis *et al*[1]). The variability of the external magnetic field is limited due to application consideration. To find a right combination, one has to resort to numerical optimization schemes. Here we provide several simulations where we manually adjust those parameters and using EGUN compute the electron trajectories.

Figure A: $R_i = 6.03758$, $R_c = 101.6$, $D_s = 0$. Output current $I = 22.73$A; Perveance $P = 1.0637$;

Figure B: $R_i = 6.03758$, $R_c = 101.6$, $D_s = 8$. Output current $I = 10.43$A; Perveance $P = 0.4881$;

Figure C: $R_i = 6.03758$, $R_c = 25.4$, $D_s = 0$. Output current $I = 15.37$A; Perveance $P = 0.7192$;

Figure D: $R_i = 6.03758$, $R_c = 101.6$, $D_s = 24$. Output current $I = 4.19$A; Perveance $P = 0.1963$.

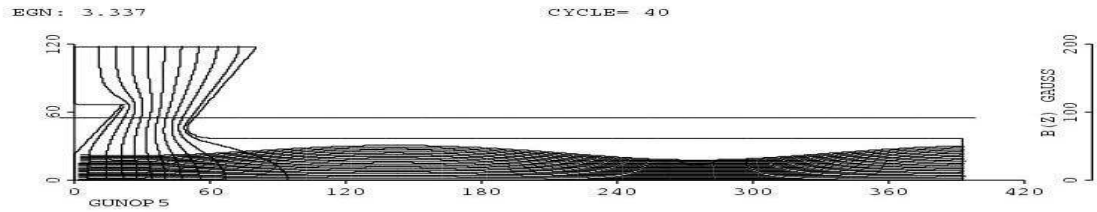

Figure 3.5.1: EGUN Simulation A

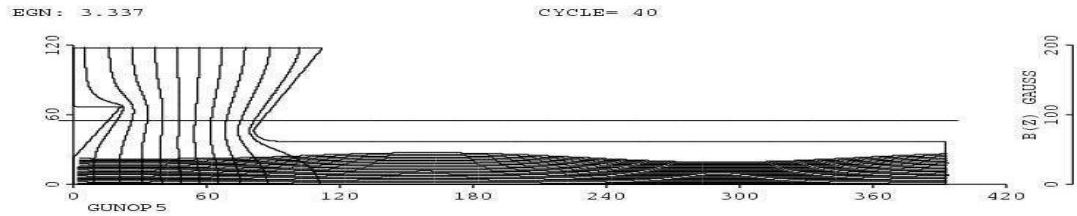

Figure 3.5.2: EGUN Simulation B

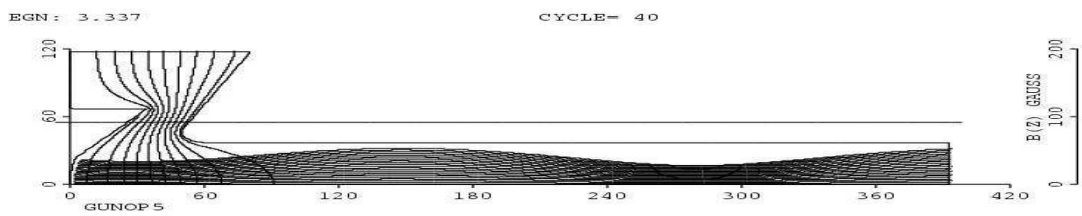

Figure 3.5.3: EGUN Simulation C

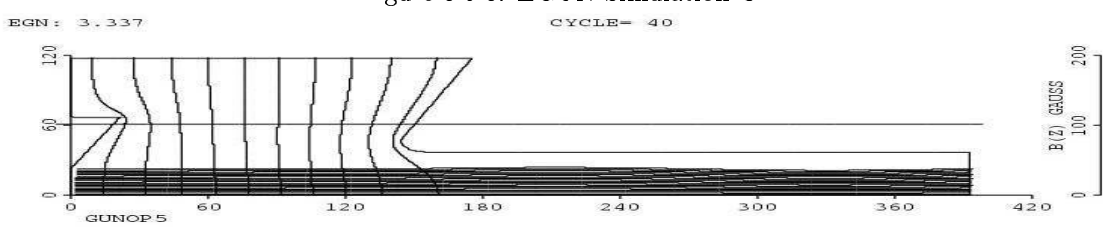

Figure 3.5.4: EGUN Simulation D

3.6 Conclusions and Possibilities for Future Work

By finding the properties of a laminar beam given a magnetic field, a significant improvement has been achieved. Electron gun designers no longer have to build the gun and then implement and adjust the magnetic field. This will conserve time, as well as improve cost by allowing for less power consumption from the solenoid. Also, we can now find a fairly good estimate for the radius of the cathode, although we still cannot find the optimal shape of the cathode.

The next step in this process would be to alter the existing optimization code to incorporate the magnetic field. This inclusion would lead to a much more efficient way to design electron guns, taking the "trial and error" of manually changing parameters in the simulations out of the process.

Bibliography

[1] Lewis, B.M., Tran, H.T., Read, M.E., and Ives, R.L., *CRSC Technical Report TR03-43*, NC State University, Raleigh NC 27695; IEEE Transactions on Plasma Science to appear.

[2] Humphries, Stan, *Charged Particle Beams*, John Wiley & Sons, 1990.

Chapter 4

PROBLEM 4: Estimating the Complexity of Event-Driven Command Sequences Executing in Parallel

Jing Cheng[1],
Sampath Kandala[2],
Ali Khoujmane[3],
Carrie Ward[4],
Mike Wilder[5],
Meng Wu[6]

Problem Presenter:
Pierre Maldague
Jet Propulsion Laboratory

Abstract

Recent discoveries in Solar System Exploration have urged scientists to implement more autonomous spacecraft. The unpredictability of such missions, as well as the autonomy that is required, makes it difficult to validate command sequences. As a result, many simulations are required in order to verify that the overall command sequence is consistent with the flight and mission rules. These command sequences are assumed to deviate from fixed-time behavior by a random but controlled parameter called the "fuzziness parameter." In this report, we will investigate the effect of the number of simulations on the consistency of the number of distinct sequences. Interpretation of this analysis will provide knowledge about how many simulation runs are appropriate for validation.

4.1 Introduction and Motivation

The Jet Propulsion Laboratory (JPL) is funded by NASA to specialize in robotic exploration of the solar system. Two powerful new rovers have been sent to Mars as part of the Mars Exploration Rover (MER) project. These rovers can be thought of as remote computers executing scripts sent to them by ground

[1]Purdue University
[2]University of Tennessee
[3]Texas Tech University
[4]NC State University
[5]UNC-Greensboro
[6]UNC-Wilmington

operations at JPL, which can be very labor intensive. As a result, a full staff is required at JPL at all times. This has created a need for a more autonomous spacecraft, which is a future mission called the Mars Science Laboratory (MSL).

In a typical script, there are three types of commands. The "fixed-time commands" are executed at a pre-determined time supplied as one of the arguments of the command, a second class of commands called "relative time commands" are to be executed as soon as the previous command terminates, and the last class called the "event-driven" commands are executed when the onboard sensors have detected a certain event. On a given sol, a Martian day, several command sequences are processed in parallel by the onboard scheduler. Therefore, the order in which commands are executed will depend on the relative speed at which the various parallel sequences are running. The reason for validation is to ensure that certain activities performed by the rover are not occurring simultaneously. For example, while taking a picture the rover should not be driving or using the robotic arm. In real operations, there are unpredictable events that are happening while these command sequences are being executed. One specific case is when the rover uses the rock abrasion tool, an early termination can occur when detecting excessive torque caused by the composition of the rock. This complicates the validation process. To make things definite, the timing of the relative-time and event-driven commands will assumed to deviate from fixed-time behavior by a random but controlled parameter called the "fuzziness parameter." In the case of relative-time commands, the amount of time it takes to execute a command will be treated as a random variable whose standard deviation will be assumed to be proportional to the fuzziness parameter.

For our analysis, we generated a baseline schedule of commands with fixed but arbitrary time durations for each activity. Then, using computer simulations we created schedules that incorporated the fuzziness parameter into a fixed baseline schedule and recorded the ending time of each activity to indicate when a command would be executed. Using a sorting algorithm on the ending times, a command sequence was created for each schedule. We were able to determine the number of distinct sequences and the frequency of each for every batch of N simulations. This insight is useful in scoping the computational requirements for a system that could validate sequences containing realistic amounts of randomness.

4.2 Model/Algorithm

The typical amount of operation time available for a rover on any given sol is about 12 Martian hours (720 minutes) in order to maximize solar power. Using a random number generator with values between 20 and 140, we generated a 6×10 matrix, which represents the baseline schedule. Each row in the generated matrix represents one type of activity performed by the rover, such as imaging, telecommunication, or driving, etc. The 10 entries in every row represent tasks to be completed within an alloted time of 20 to 140 minutes. Each row sum may exceed 720, however, these additional tasks may be completed after adding randomness to the schedule.

Equation (1) models the baseline schedule with added randomness:

$$t(A_{ij}) = T(A_{ij})(1 + \phi \cdot X(A_{ij})). \tag{4.2.1}$$

A_{ij} corresponds to the task in the ij^{th} entry of the baseline matrix, i is the activity, and j is the task for that activity. The nominal time, $T(A_{ij})$, is the ij^{th} entry of the baseline matrix. ϕ is defined to be the random but controlled fuzziness parameter and $X(A_{ij}) \sim \mathcal{U}(-1, 1)$ adds randomness to the baseline matrix. We define $t(A_{ij})$ as the matrix of randomized operation times for each task.

Using Matlab and C programs, we calculated the cumulative time of the tasks for each activity. This allowed us to sort the ending times and then create the final command sequence for the schedule with the fuzziness parameter. From here, we ran several simulations repeating this procedure for a fixed baseline.

4.3 Validation of Algorithm

To validate the algorithms, we fixed the baseline, $\phi = .005$, $N = 2,000$, and each time changed only the random variable $X(A_{ij})$. Figures 1-3 provide the validation for these algorithms.

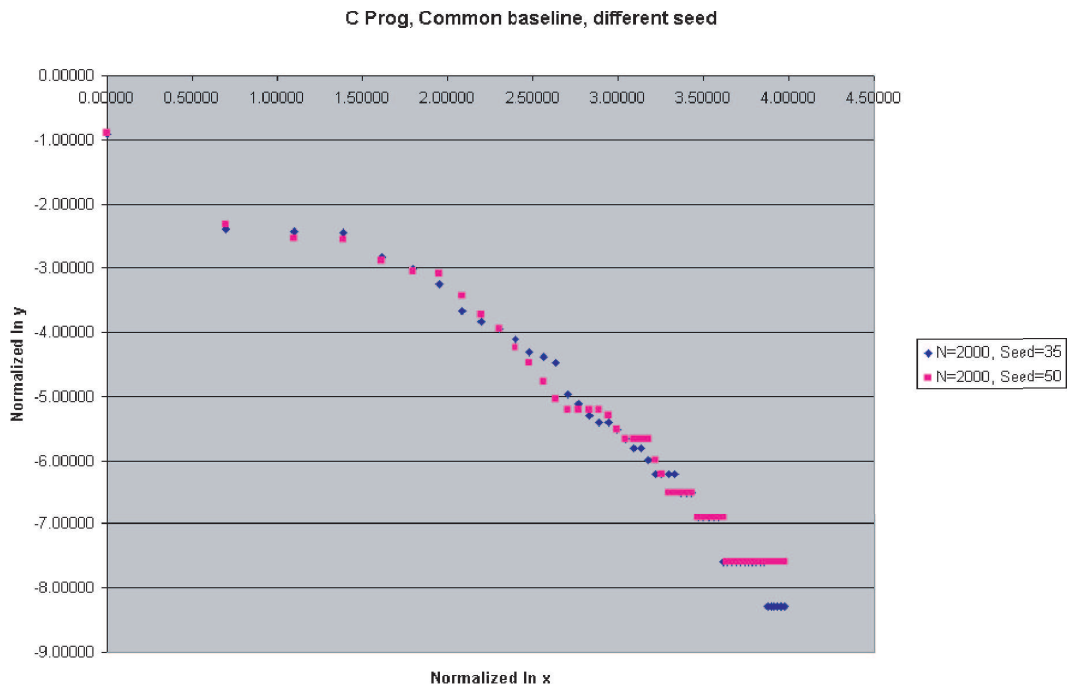

Figure 4.3.1: Validation of the C Program

4.4 Results

Initially, we fixed $\phi = .2$ and ran N simulations, however, our results showed N distinct sequences. In this case, we could not choose a large enough N due to computational limitations to get an interesting distribution for the sequences. So, we needed to find a realistic range for ϕ.

After a few trials, we discovered that $\phi = .005$ is more realistic for computational purposes.

From Figure 4, it is clear that when $\phi = .05$ and $\phi = .5$ there are many distinct sequences that do not occur often. At the same time, when $\phi = .0005$, there is only one distinct sequence. Furthermore, $\phi = .005$ and $\phi = .01$ produce many distinct sequences that occur at various frequencies. So, from this point on we will work with $\phi = .005$ and $\phi = .01$ for our analysis.

Now that we have certain choices for ϕ, we looked at how the frequency curve changes with N.
As shown in Figure 5, there is a translation by a vertical shift between each frequency curve. This led us to discover a normalization for the log of the frequency and the log of the number of distinct sequences.

Figures 6 and 7 display the normalized plots, $\log(\frac{y}{N^\beta})$ vs. $log(\frac{x}{N^\alpha})$. Using $\alpha = 0$ and $\beta = 1$, the graphs demonstrate the best convergence of the frequency curves.

Clearly, as we increase N, the number of distinct sequences increases as well, which will eventually reach a maximum of 60!. Therefore, it is necessary to define a cut-off point for our measure of complexity. Using the equation below, we defined our cut-off point to be X_α.

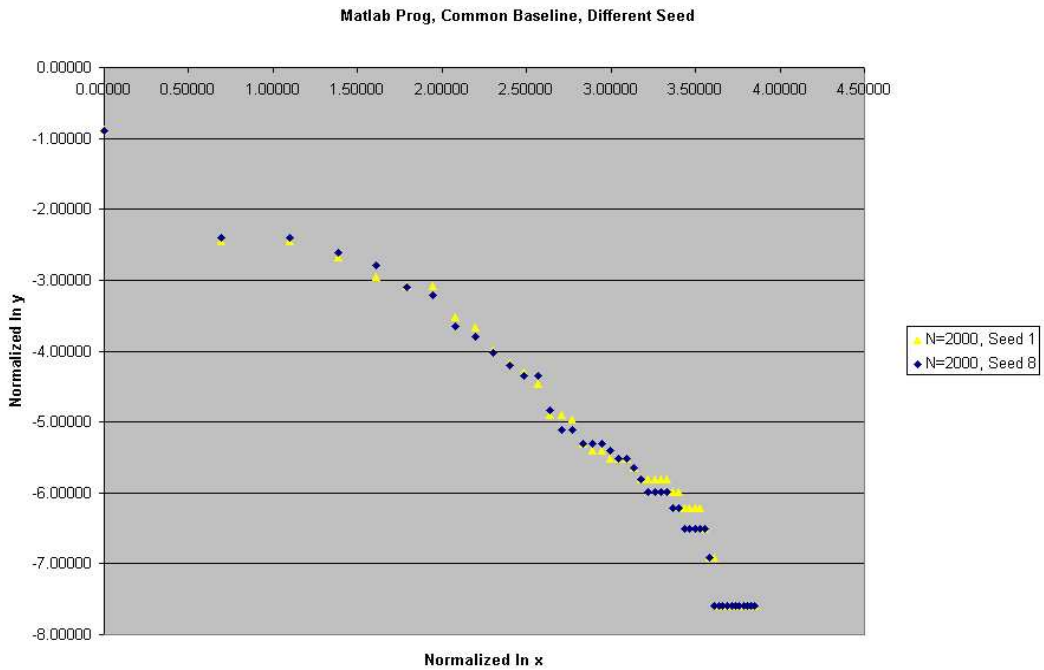

Figure 4.3.2: Validation of the Matlab Program

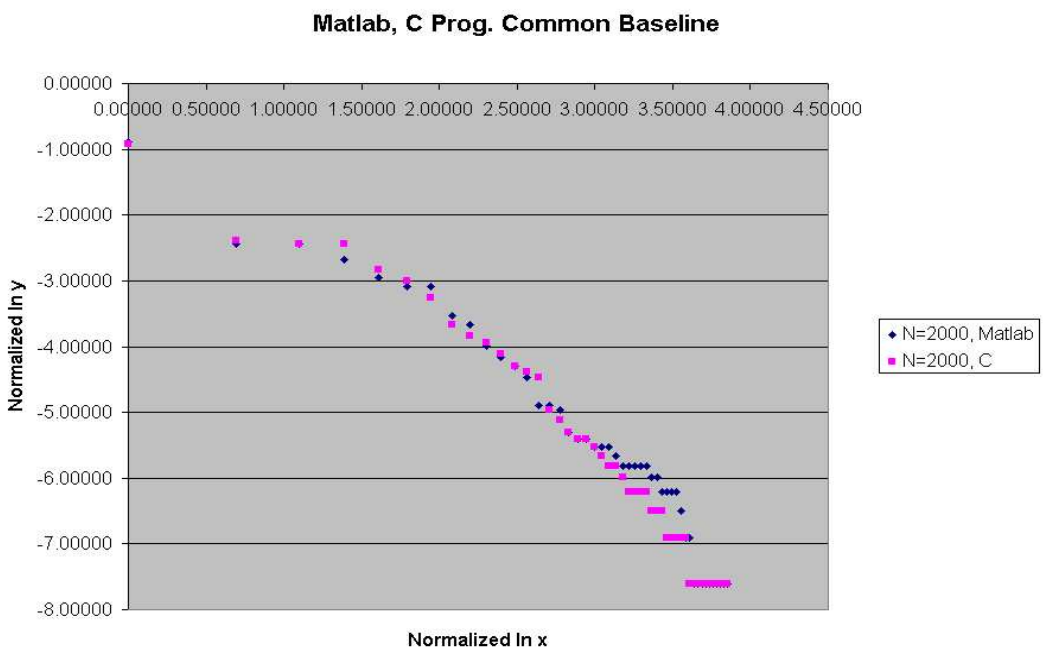

Figure 4.3.3: Validation of Matlab vs. C

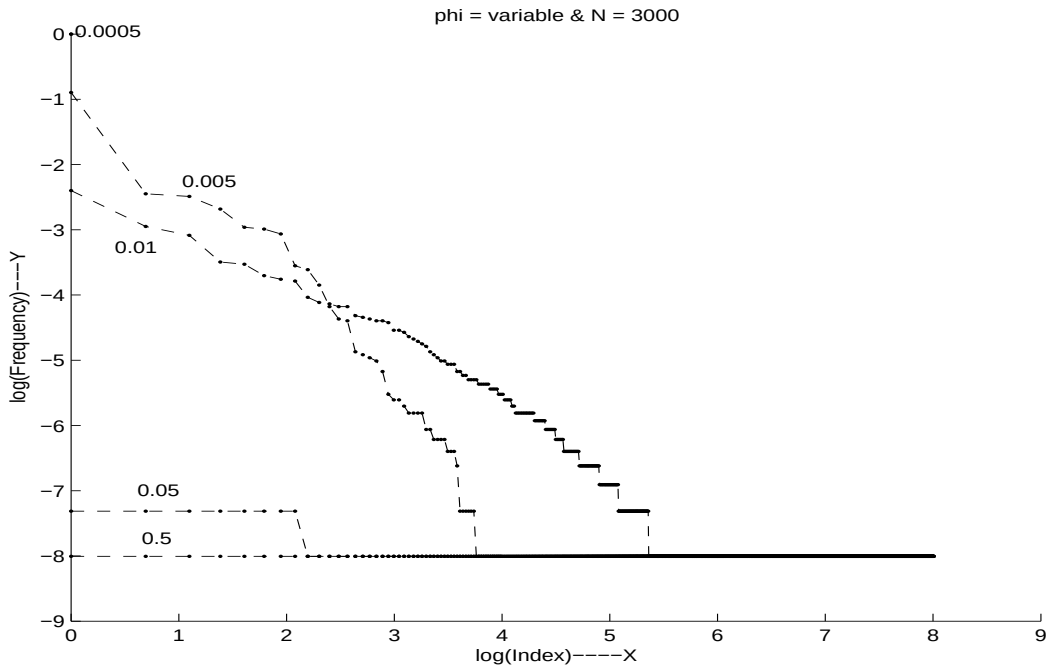

Figure 4.4.1: Log-Log Plot of Frequency vs. Sequences Ids(Index) for a Fixed $N = 3000$ Simulations and Varying ϕ

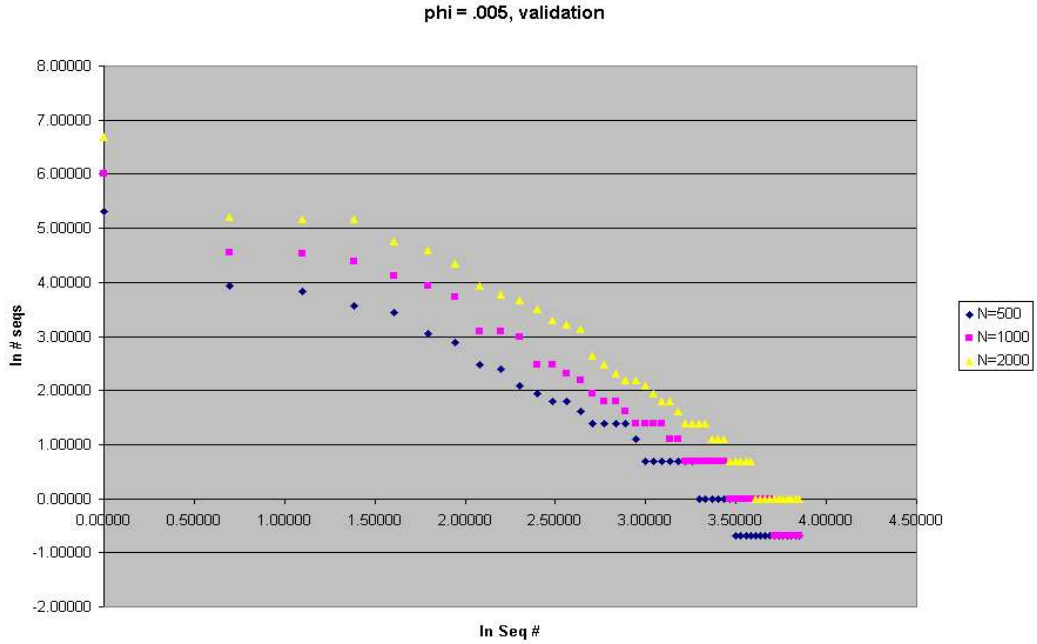

Figure 4.4.2: Log-Log Plot of Frequency vs. Sequences Ids(Index) with Varying N Simulations and a Fixed $\phi = .005$

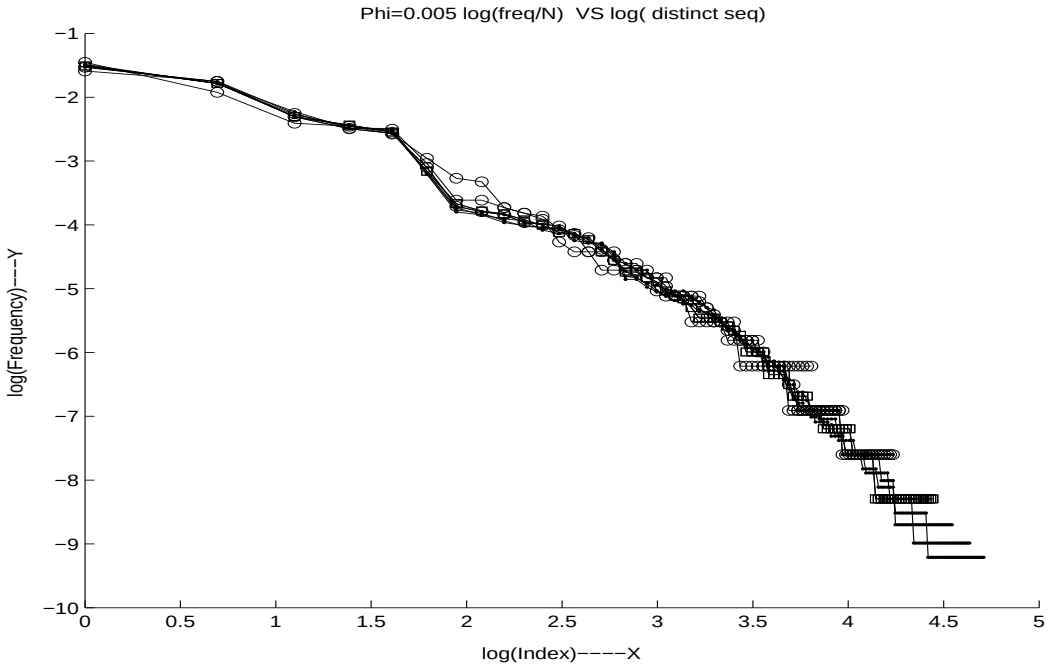

Figure 4.4.3: Normalized Log-Log Plot of Frequency vs. Sequences Ids(Index) with Varying N Simulations and a Fixed $\phi = .005$

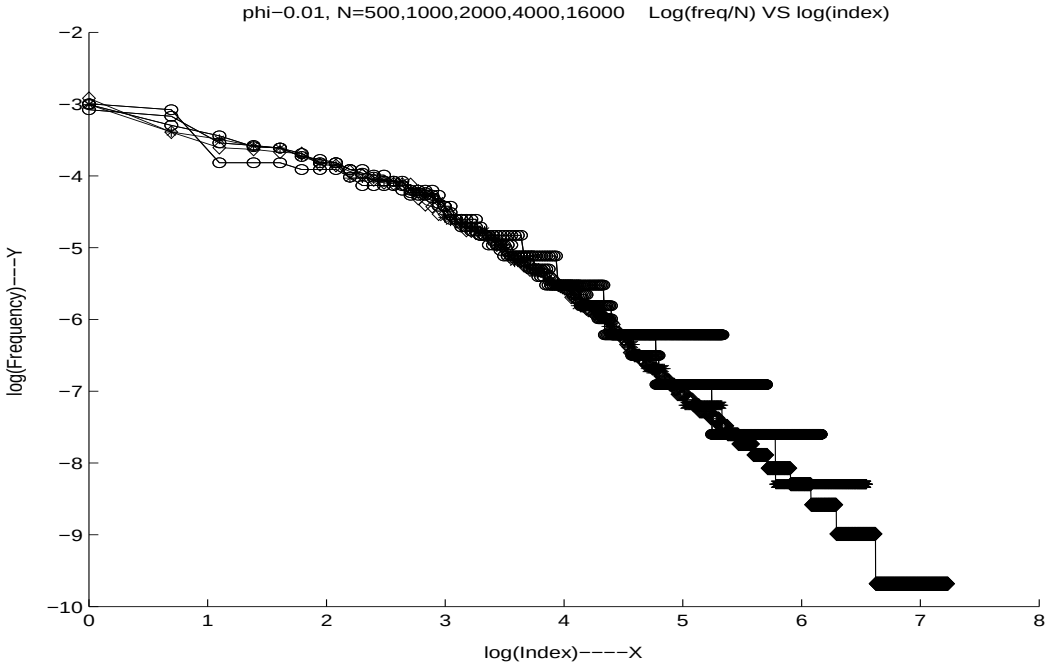

Figure 4.4.4: Normalized Log-Log Plot of Frequency vs. Sequences Ids(Index) with Varying N Simulations and a Fixed $\phi = .01$

$\phi = .01$	N	X_{max}	$X_{.95}$	$X_{.80}$
	500	207	182	107
	1000	299	249	109
	2000	474	375	132
	4000	697	498	145
	8000	980	581	155
	10000	1086	587	152
	16000	1384	668	156
	20000	3084	668	156
$\phi = .005$	500	45	25	10
	1000	53	26	11
	2000	69	29	11
	4000	85	29	11
	6000	94	29	12
	8000	103	29	11
	10000	111	29	11
	20000	132	28	11

Table 4.4.1: Measure of Complexity

$$X_\alpha \equiv \max_J : \sum_{i=1}^{J} \frac{y_i}{N} \leq \alpha \tag{4.4.1}$$

where $J \leq X_{max}$, the number of distinct sequences, and α is the desired percentage (decimal) of distinct sequences being represented.

Initially, we looked at $\alpha = .95$, as displayed in Table 1, however, $X_{.95}$ does not saturate fast enough. By reducing $\alpha = .80$, we get faster convergence.

Our results from Table 1 are plotted in Figures 8 and 9 and the overall relationship between X_{80} and ϕ is depicted in Figure 10.

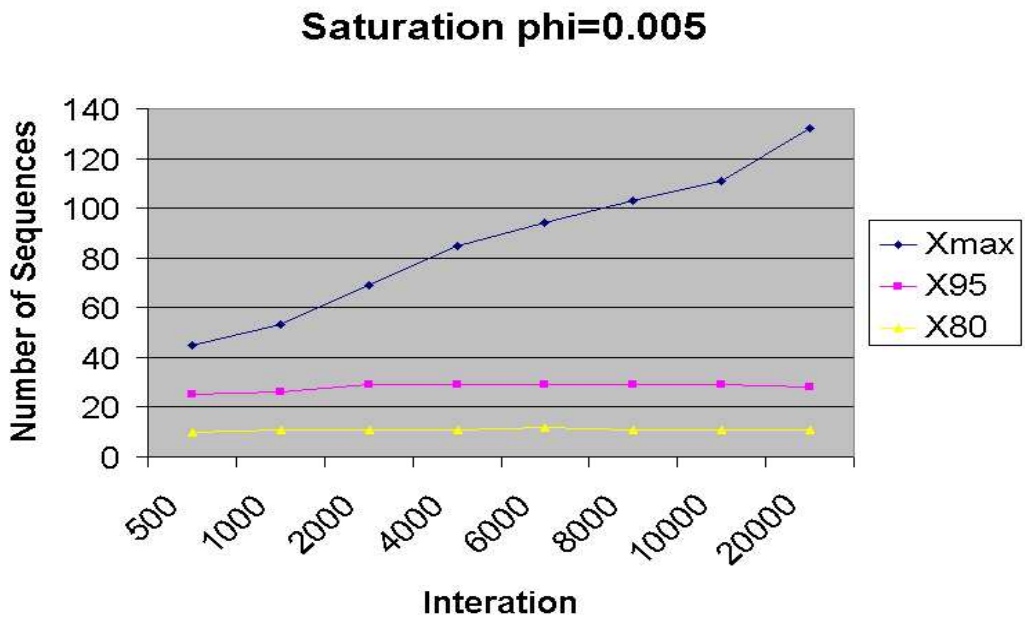

Figure 4.4.5: Saturation Rate of $X_{.80}$ for Different N Values and $\phi = .005$

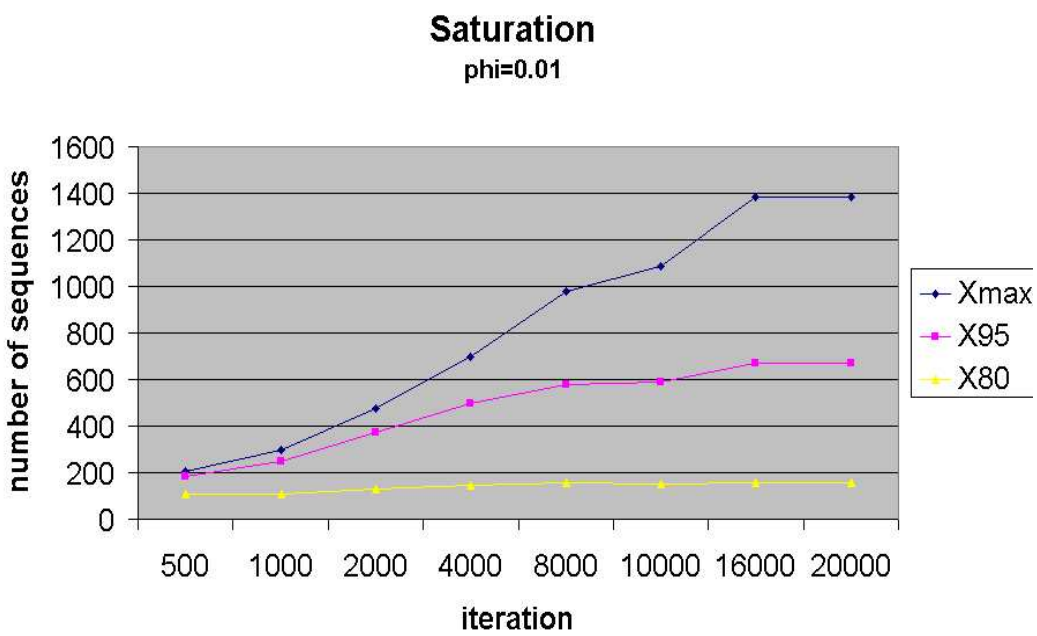

Figure 4.4.6: Saturation Rate of $X_{.80}$ for Different N Values and $\phi = .01$

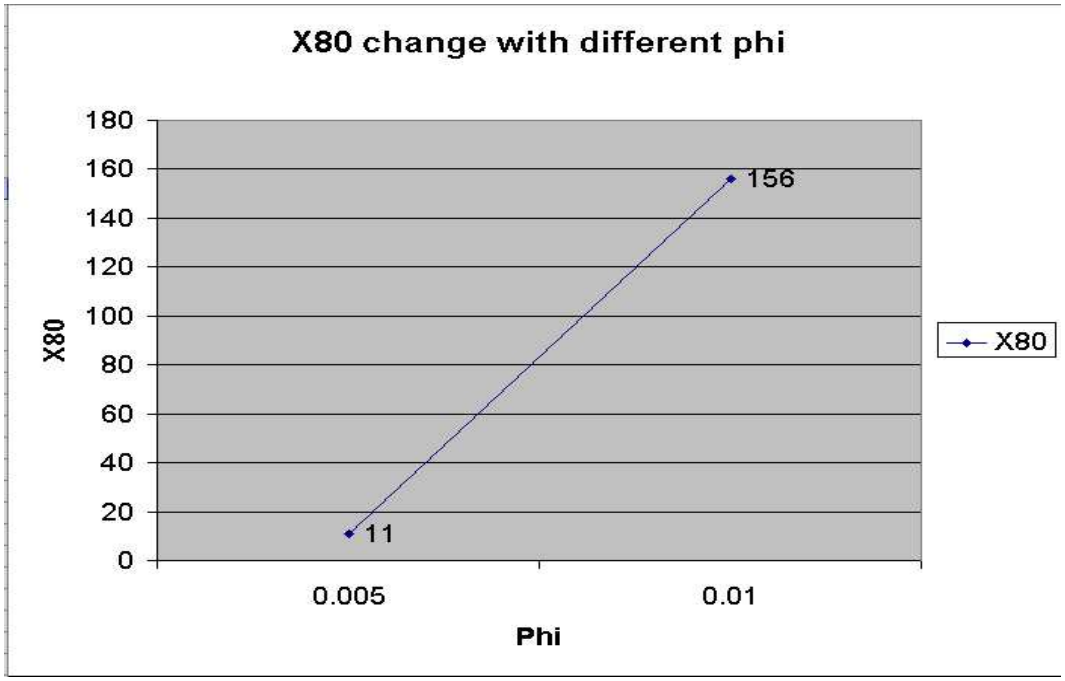

Figure 4.4.7: $X_{.80}$ vs. Different ϕ Values

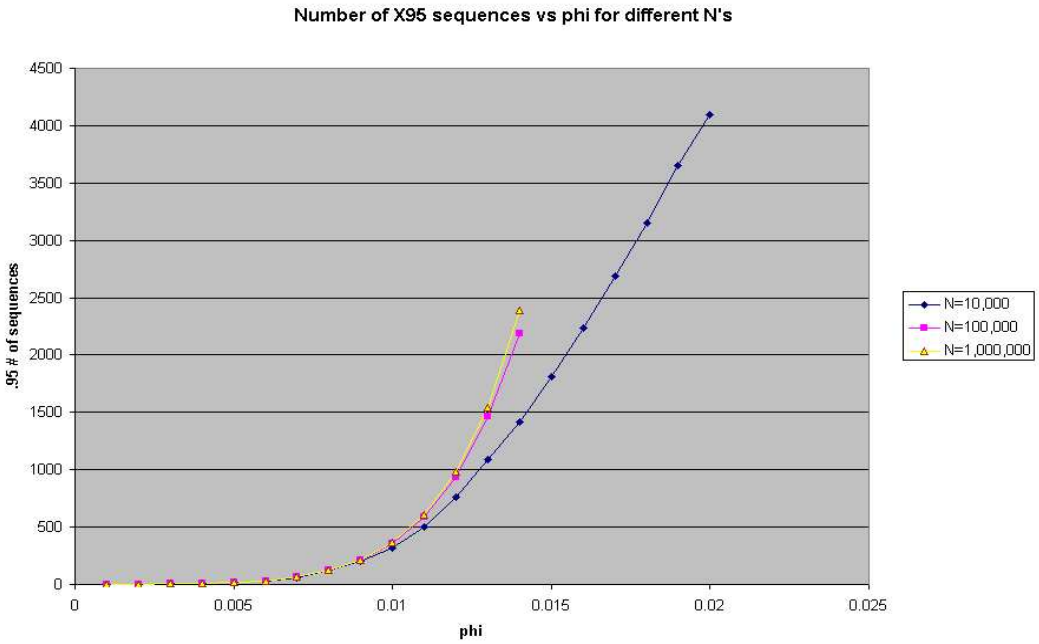

Figure 4.4.8: $X_{.95}$ vs. ϕ for N Values

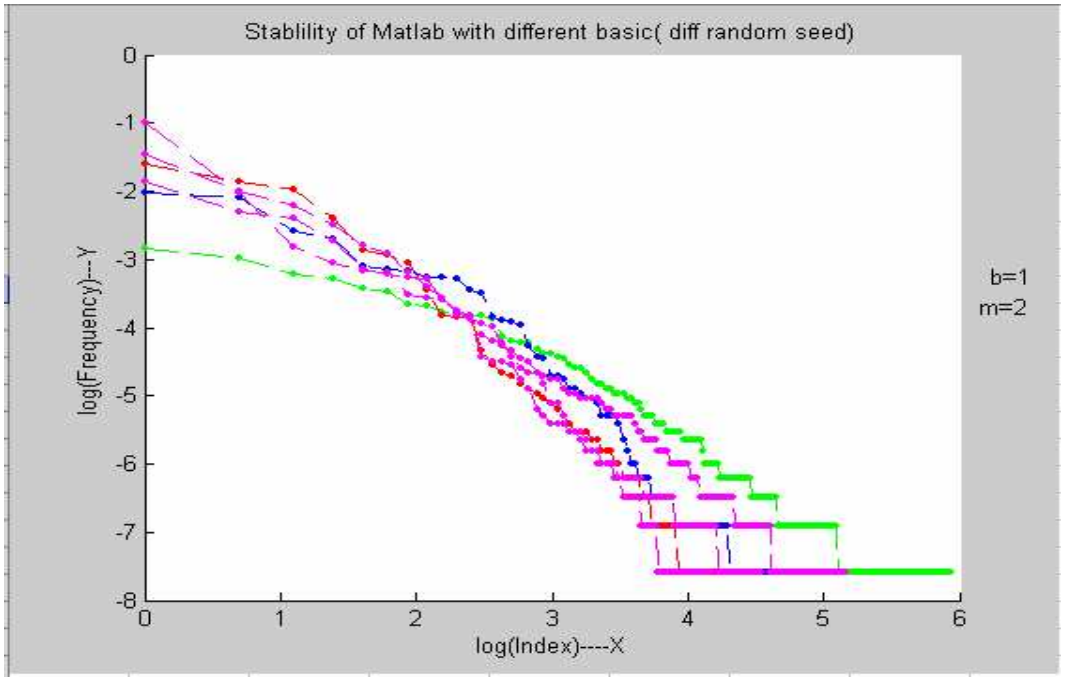

Figure 4.4.9: Frequency Curves for Different Baselines and for $\phi = .01$ and $N = 2000$

4.5 Conclusions and Future Work

We have investigated certain aspects that contribute to the complexity of command sequences executing in parallel. Initially, we narrowed down a range for ϕ that is suitable for computational purposes, Figure 11 also captures this notion. Also, we have discovered an appropriate value for N at which the number of distinct sequences saturates. Some of our results indicate that the frequency curves are sensitive to the baseline matrix and consequently needs future investigation, as seen in Figure 12. In addition, revisiting our assumptions that every activity is random would be beneficial since in actual operations only some activities are random. For example, telecommunications is an activity dictated by the time available on the Deep Space Network, therefore, this is an activity that could have a fixed time duration. Another point of interest would be to investigate how the probability distribution of our random matrix, $X(A_{ij})$, contributes to the complexity.

4.6 Acknowledgements

We would like to thank Dr. Pierre Maldague for his insight and guidance in our research. We would also like to thank our faculty consultants, Dr. Tao Pang and Dr. Robert Buche.

Bibliography

[1] Jet Propulsion Laboratory webpage, Current Missions–2003 Mars Exploration Rovers.

http://www.jpl.nasa.gov/missions/current/marsexplorationrovers.html (accessed July 2004)

Chapter 5

PROBLEM 5: Identifying Respiratory Parameters from Plethysmography Data

Miyuki Breen[1],
Zheng Chen[2],
Bree Ettinger[3],
Subhrangshu Nandi[4],
Brenda Tapia-Santos[5],
Heather Wilson[6]

Problem Presenters:
Paul Schlosser, Brian Wong
CIIT Centers for Health Research

Annie M. Jarabek
US EPA Visiting Scientist
CIIT Centers for Health Research

H. Joel Trussell
Electrical and Computer Engineering
NC State University

Mette Olufsen
Math Department
NC State University

Mansoor Haider
Math Department
NC State University

Abstract

[1]Case Western Reserve University
[2]Florida State University
[3]University of Georgia
[4]University of Massachusetts
[5]Centro de Investigacion en Matematicas
[6]University of Central Florida/NCSU

CIIT wanted to obtain a more accurate analysis for comparing normal breathing of rats to the aggravated breathing, which occurs when the rats are exposed to chlorine gas. CIIT is currently using the Buxco system. The rat is placed in a plethysmograph coupled with a "black box" software package that utilizes a model by Drorbaugh and Fenn, which selects "good" breathing signals and then calculates tidal volume and breathing frequency. The problem with the "black box" software is that CIIT does not know how it is choosing the signals that represent the breath. The goal of this project was to develop a program which CIIT can use to understand how the signals which represent the breaths are being distinguished from noise.

During the workshop we developed a model for filtering data and implemented a model that rejects "bad" data and accepts "good" data. CIIT's current raw data before chlorine exposure and current criterion were used to accept "good" data and reject "bad" data. Good data represents breathing and "bad" data represents noise such as scratching and movement. In addition, we developed a dynamic flow model that can calculate the tidal volume and frequency using filtered data. Once noise was filtered and the dynamic flow model was run, the findings were compared to CIIT's findings. It is our hope that CIIT will be able to use the results and make further modifications as needed.

5.1 Introduction and Motivation

The CIIT Centers for Health Research (CIIT) was founded in 1976 and has since evolved to become "a renowned leader in environmental health sciences research and education"[3]. CIIT was created by 11 leaders of major chemical companies to address growing concerns on the effects of chemicals relating to environmental and human health. One of CIIT's main sources of funding is the American Chemistry Council (ACC). There is a strong emphasis on being unbiased in reporting their scientific findings. CIIT is a private non profit company located in Research Triangle Park, NC. In the 1990's, CIIT added risk assessment into their research. This helped the company become a collaborator with scientists and governments world-wide. In the 21st century CIIT adapted their "systems biology approach". This approach combines functional genomics, computational biology, and bioinformatics.

The CIIT Centers for Health Research and the U.S. Environmental Protection Agency are interested in developing a risk assessment for human exposure to airborne chlorine. In particular, they wish to estimate the risk or probability of an adverse health effect as a function of exposure level. The respiratory tract is a primary entry way for inhaled toxins, which have many adverse affects such as destroying lung tissue and altering breathing patterns. Several pulmonary function tests can be implemented to analyze the integrity of the respiratory tract; whole-body plethysmography is just one example[3].

Whole-body plethysmography is the study of respiration dynamics in animals by measuring the pressure changes of a sealed chamber encasing the animal. Through whole-body plethysmography one can collect the frequency and the volume of the breath. When an animal inhales it heats and humidifies the air it inspires. The pressure in the chamber increases since the warm humid air has a greater volume than the same amount of the original air. During exhalation, the process is reversed. In an experiment the animal is not constrained so they may sneeze, scratch, sniff, or move around the chamber. All these actions affect the animals breathing and show up in the data as noise, which may change the pressure in the chamber complicating the analysis of the experiment.

In the current experiment at CIIT, a rat is placed in a calibrated plethysmography chamber. After the animal is given time to acclimate to the chamber, chlorine gas is pumped into the top of the chamber. To maintain an equilibrium in the chamber, air is drained from the bottom of the chamber and through pneumotacs at the top of the chamber. A sensor reads the pressure changes of the chamber and outputs raw data in volts. The voltage changes are proportional to the pressure changes in the system; thus, indirectly measuring the inspiratory and expiratory flows. The raw data is then run though BioSystem's XA software which provides a "black box" analysis of the data by using what is believed to be the Drorbaugh and Fenn model for whole-body plethysmography[4].

During the workshop, we developed a program that filters the data and implements a traditional (pseudo-static) model and a dynamic flow model. First, we filtered the noise out of the original data using a Butterworth filter with passband of 3 Hz and stopband of 10 Hz. Then, we implemented a criteria to accept data representing good breaths and reject data that represents the bad breaths or noise. The Drorbaugh and Fenn model was then applied. Next, we developed a dynamic flow model with fewer assumptions than the Drorbaugh and Fenn model. The model was tested on both the raw data and filtered data before chlorine exposure, and our results were compared to CIIT's current results.

5.2 Signal Processing

Signal processing is a method of analyzing data and filtering out unwanted properties in signals. The goals of signal processing performed in this project were to filter out unwanted signals from the data obtained from CIIT's experiments and apply the current criteria for a "good breath" to examine any effect from background signal to accurately detect good breaths. We considered data from both an empty and an occupied chamber before chlorine exposure.

The Fourier Transform has played a key role in signal processing due to its wide range of applications, including signal filtering and analysis. The Fourier transform simply changes the signal from the time domain to the frequency domain. For a continuous signal that was discretized in a sequence $f(x)$ by taking N samples Δx units apart, the discrete Fourier Transform is given by

$$F(u) = \frac{1}{N}\sum_{x=0}^{N-1} f(x)\exp(\frac{-i2\pi ux}{N}) \tag{5.2.1}$$

for $u = 0, 1, 2, , N-1$.

Based on Euler's formula,

$$\exp(\frac{-i2\pi ux}{N}) = \cos(\frac{2\pi ux}{N}) - i\sin(\frac{2\pi ux}{N}), \tag{5.2.2}$$

$F(u)$ is composed of a sum of sine and cosine terms, and each value of u determines the frequency of its corresponding sine-cosine pair. This frequency domain representation of the signal is often useful to perform signal filtering and analysis.

Filtering is a signal processing method to remove an undesirable signal (such as noise) from the data. In the frequency domain, instead of the time domain, the filtering process is straightforward. We simply compute the Fourier transform of the signal to be filtered, multiply the result by the filter's transfer function (Fourier transform of the filter's impulse response), and take the inverse Fourier transform to produce the filtered signal. In our application, rapid transitions in the voltage levels of the signal (noise) contribute significantly to the high frequency content of the signal's Fourier transform. Hence, a smooth low frequency signal can be achieved in the frequency domain by attenuating a specific range of high frequency components in the Fourier transform of the signal.

First, we used data from CIIT's experiments with an occupied chamber, which we filtered. Once we had filtered the data, we looked for the areas on the graphs believed to be breathing. From looking at the data we estimate that breathing occurs around 1 Hz. We used a low-pass butterworth filter with a transition band of 3-10 Hz to preserve the 1 Hz signal and its harmonics. We were then able to detect noise that had previously gone undetected. To examine any effect from the background noise of the empty chamber, we qualitatively compared the signal from the empty and occupied chambers. Significant background noise was observed from the empty chamber, which had a similar frequency and pattern as the breathing signal. Therefore, we were unable to eliminate this background noise with our current low-pass filter design. The separation of the respiratory signal from the background noise will require a more sophisticated filtering method. Since it was

observed that the amplitude of the respiratory signal was significantly higher than the background noise. We expect the noise to have a minimal effect on our results.

Figure 5.2.1 shows a comparison between the raw and filtered data with an occupied chamber. The filtered data appears much smoother than the original data since we eliminated the high frequency noise. We believe that we successfully eliminated noise while preserving the breathing signal, since the filtered signal displays the characteristics expected from breathing before chlorine exposure.

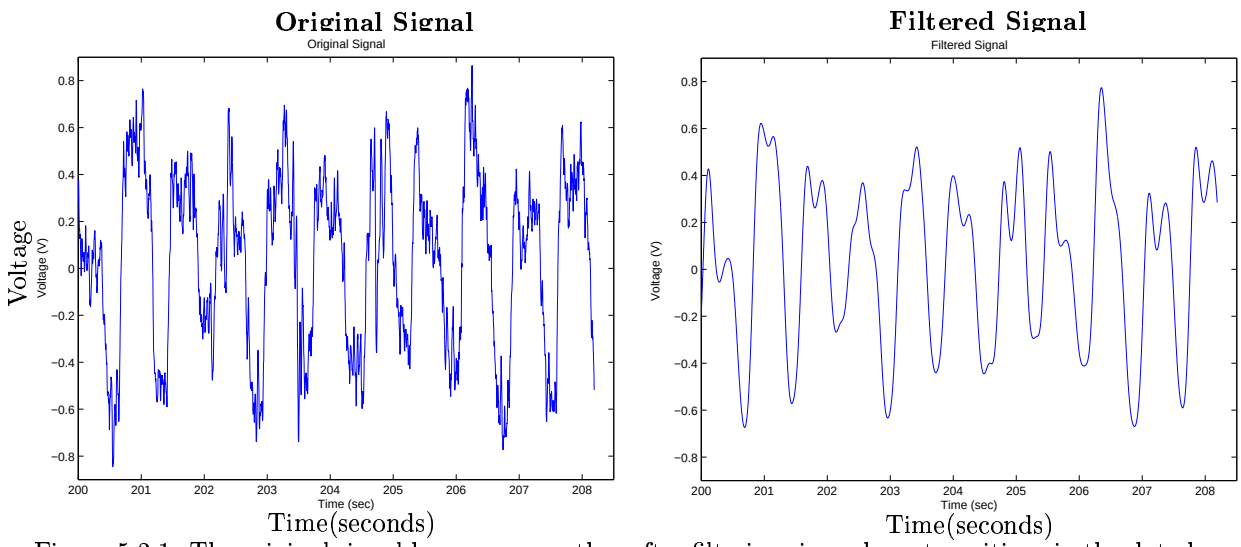

Figure 5.2.1: The original signal becomes smoother after filtering since sharp transitions in the data have been significantly removed.

We transformed data in Figure 5.2.1 from the time domain to the frequency domain as shown in Figure 5.2.2. We can see that the high frequency noise has been effectively eliminated. Figure 5.2.3 is a comparison of spectrograms before and after filtering data from an occupied chamber in order to examine the harmonics, which are necessary to detect the breathing pattern. The breathing is believed to occur between 1 and 2 Hz. Above the 2 Hz we observe approximately three distinct horizontal bands that represent the harmonics of the fundamental component of the breathing signal. The spectrograms demonstrate that the harmonics were preserved by the filtering process since the bands of the harmonics are clearly evident in the filtered signal's spectrogram.

5.3 A "GOOD" Breath

In theory a good breath looks as shown in Figure 5.3.1 where IT is the inhalation time, V_I represents the estimated volume change of the lung during inhalation, and V_E represents the estimated volume change during exhalation.

A "good" breath should have an inhalation time (IT) greater than 0.1 second but less than 4.0 seconds. The volume balance should be no greater than 40% [10], i.e.

$$\frac{(V_I - V_E)}{V_I} \leq 0.40. \tag{5.3.1}$$

Using this criterion, we can then select "good" breaths. We took part of a signal and applied the criteria of a good breath which resulted in Figure 5.3.2.

We are also interested in calculating the tidal volume of the breath. First we need to convert the voltage into pressure. To do this we use the equation:

$$P = \frac{V}{K_p} \qquad \text{where} \qquad K_p = \frac{V_O}{V_k}\int_0^T v_k dt. \tag{5.3.2}$$

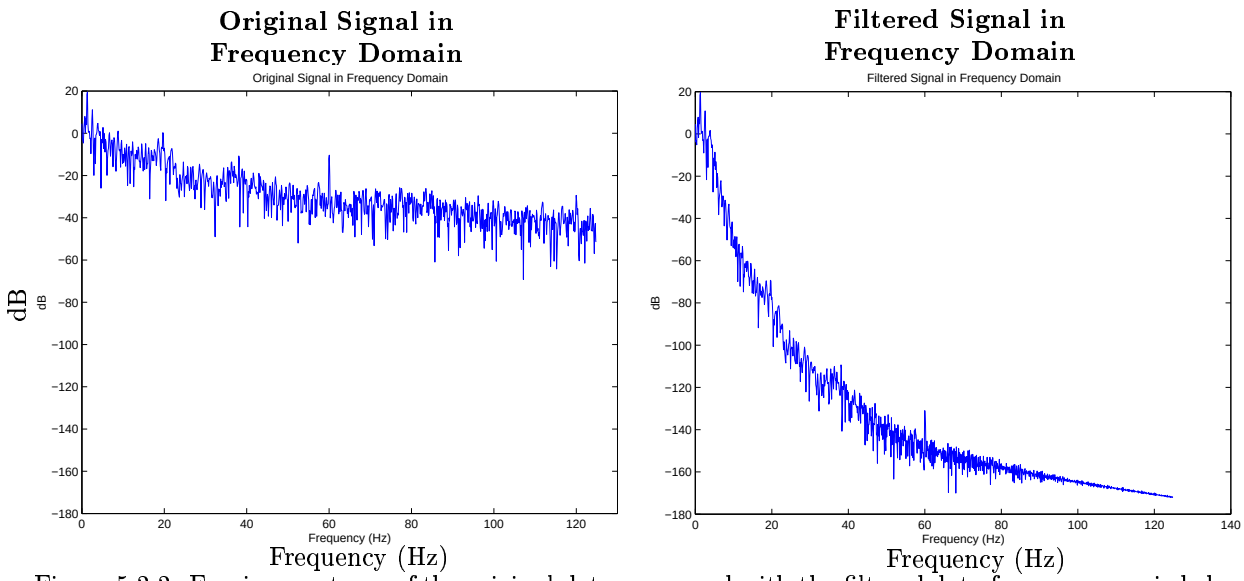

Figure 5.2.2: Fourier spectrum of the original data compared with the filtered data from an occupied chamber.

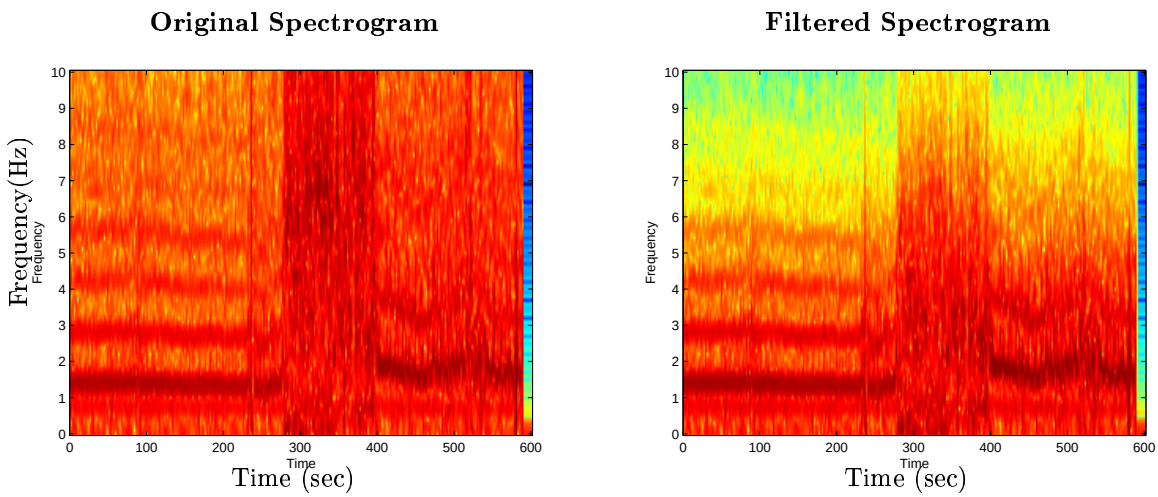

Figure 5.2.3: Spectrogram of original signal compared with the filtered signal from an occupied chamber. The breath is believed to occur between 1 and 2 Hz. Harmonics of the breath are shown at a higher frequency.

V_O to represents the volume of the chamber (3900mL), V_k represents a calibration volume of 3 mL, and v_k represents the calibration voltage output. The tidal volume is calculated using an extension of the Drorbaugh and Fenn model, as follows:

$$V_T \left[\frac{P_{atm} - P_o^v}{T_o} - \frac{P_{atm} - P_i^v}{T_i} \right] = \frac{V_k P_{atm}}{T_o} \frac{\int_0^T v \, dt}{\int_0^T v_k \, dt} \tag{5.3.3}$$

To compute the tidal volume, we numerically calculated the integral in Equation (5.3.2) and (5.3.3) across time using trapezoidal integration. The tidal volume will be used during the derivation of the dynamic flow model described in Section 4.

Figure 5.3.3 gives the tidal volumes from our calculations compared with the tidal volumes obtained with results using the "Black Box" software. It is clear that our calculated tidal volume differs significantly from the tidal volume determined by the "Black Box" software. It is possible that we could improve the performance of our filter to more effectively remove high-frequency noise for better estimates of the tidal volume. However, this modification would result in only a small change in the tidal volume. We observed that our results were

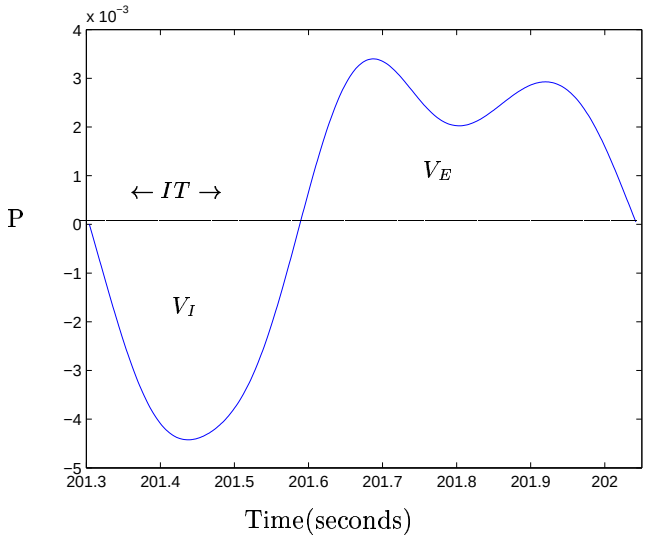

Figure 5.3.1: This is an example of what a "good" breath would look like in a plot of pressure versus time. V_I and V_E represent the estimated volume change of the lung during inhalation and exhalation and IT represents the inhalation time.

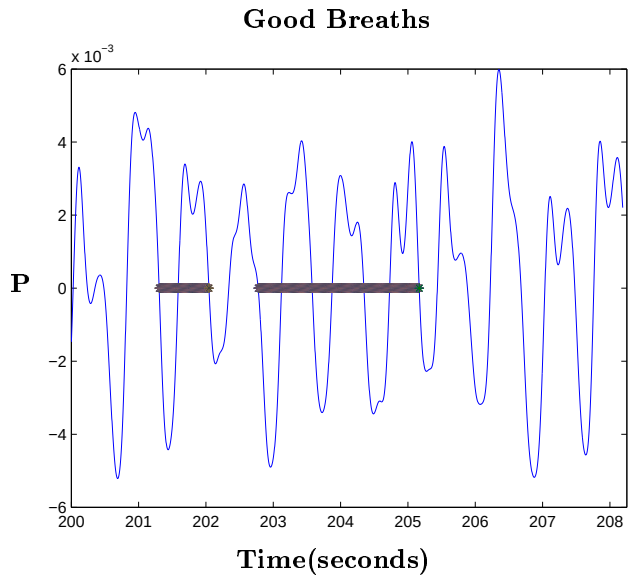

Figure 5.3.2: The horizontal lines represent the breaths, determined by Equation (5.3.1). We have chosen just part of a breathing signal before chlorine exposure to illustrate what would be chosen versus what would be discarded.

approximately three times smaller than the values for the "Black Box" software. This observation leads us to believe that we specified an incorrect value for one of the constants in our model.

5.4 Extension of Drorbaugh and Fenn Model

To obtain the dynamic flow model we start by describing an extension of the Drorbaugh and Fenn model. In this extension some of the assumptions of the original Drorbaugh and Fenn model were modified. Below is a

Tidal Volumes

Group 5	"Black Box"
0.4362	1.24
0.5161	1.30
0.3624	1.10
0.4434	1.20

Figure 5.3.3: We compare the tidal volumes from our calculations to the calculation done by CIIT.

diagram of the chamber illustrating the chamber and variables included in our extended Drorbaugh and Fenn model (see Figure 5.4.1).

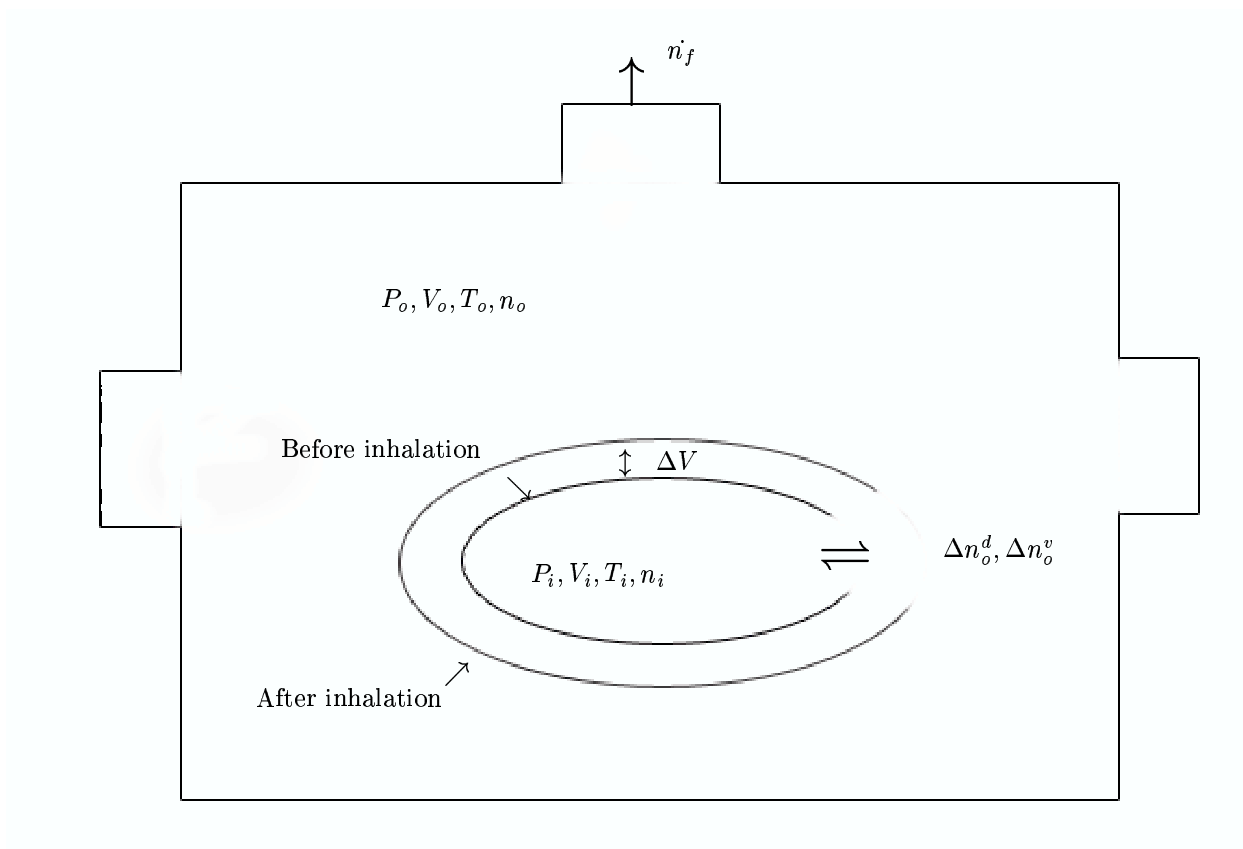

Figure 5.4.1: Extention of the Drorbaugh and Fenn Model, diagram of the chamber initially. T_0 and T_i is the temperature within the chamber and in the animal, P_0 and P_i is the final vapor pressure and the saturation with water vapor for T_i, V_0 and V_i are the volume of the chamber outside the animal and the volume of air inside the animal, Δn_0^d and Δn_0^v are the changes in the number of dry air molecules and the water vapor molecules in the chamber, and n_i is the total number of air molecules in the lungs.

As in the Drorbaugh and Fenn model we study an animal placed in a closed chamber at room temperature. The flow of heat from the animal will warm the interior of the chamber and initiate a flow of heat from the chamber to the room. When the rates of heat exchange between the box and the animal are equal, equilibrium will be established. In this extension of the Drorbaugh and Fenn model we will consider the flow of gas molecules through the opening, which we will denote by $\dot{n_f}$. Let us define:

T_o	The temperature within the chamber
T_i	The body temperature of the animal
P_i	Saturation with water vapor for T_i
P_o	The final vapor pressure

From the Drorbaugh and Fenn model we have that as the animal breathes in, it inspires air at temperature T_o and at vapor pressure P_o. At the end of inspiration, a volume of air which we have assumed to be approximately equal to the volume of the inspired air is present at temperature T_i and pressure P_i. That volume of air which is now at T_i and P_i will thus be present at a higher pressure because of added heat and water vapor than prior to inspiration. This increased pressure will be transmitted to all parts of the chamber and the resulting increase in pressure within the chamber may be represented by P. In this model we are considering that the moment when inspiration ends and expiration begins is identical with the time when the chamber pressure returns to atmospheric; i.e. when $P = 0$. So, the voltage curve has gone down through it's minimum and returned to zero. At this point we have the equation:

$$\frac{V_o(P_{atm}-P_o)}{T_o} + \frac{V_i(P_{atm}-P_i)}{T_i} = \frac{(V_o-V_T)(P_{atm}-P_o)}{T_o} + \frac{(V_i+V_T)(P_B-P_i)}{T_i} + R * n_f \tag{5.4.1}$$

In (5.4.1), V_o equals the volume of the chamber outside the animal, V_i equals the volume of air inside the animal, to which the tidal volume V_T is added, n_f is the net number of molecules that have flowed out of the chamber through the pneumotacs and P_{atm} is the atmospheric pressure. Rearranging (5.4.1) we get

$$V_T\left[\frac{(P_{atm}-P_o)}{T_o} - \frac{(P_{atm}-P_i)}{T_i}\right] = R * n_f \tag{5.4.2}$$

The rate of flow of gas molecules through the opening is proportional to the pressure difference between the chamber and the atmosphere. Thus, in a small time Δt

$$\begin{aligned} \Delta n_f &= K_r(P_o + \Delta P - P_{atm})\Delta t \\ &\approx K_r(P_o - P_{atm})\Delta t && (5.4.3) \\ &= \frac{K_r}{K_p}v && (5.4.4) \end{aligned}$$

Integrating (5.4.3) we obtain:

$$n_f = \frac{K_r}{K_p}\int_0^T v dt \tag{5.4.5}$$

From $PV = nRT$ and considering that during the calibration injection, the volume injected is V_k and this is due when the animal is not in the chamber, we obtain

$$n_k = \frac{P_{atm}V_k}{RT_o} = \frac{K_r}{K_p}\int_0^{t_k} v_k dt \tag{5.4.6}$$

where v_k the voltage of the calibration and t_k is the time at which the pressure signal from the calibration returns to 0. Remember, the calibration does not involve the presence of the animal into the chamber, so the temperature involved in this process is T_o. From (5.4.6) we obtain $\frac{K_r}{K_p}$ and hence, from (5.4.5) we have

$$n_f R = \frac{P_{atm}V_k}{T_o}\frac{\int_0^T v\,dt}{\int_0^{t_k} v_k\,dt} \tag{5.4.7}$$

Substituting (5.4.7) into (5.4.2), we get the expression

$$V_T \left[\frac{P_{atm} - P_o^v}{T_o} - \frac{P_{atm} - P_i^v}{T_i} \right] = \frac{V_k P_{atm}}{T_o} \frac{\int_0^T v\, dt}{\int_0^{t_k} v_k\, dt} \tag{5.4.8}$$

Again, this applies at t_k, the time at which the pressure signal from the calibration returns to 0. T is the time at which the pressure signal from the breath returns to zero. Since during inhalation and calibration injection both signals go negative, both of the integrals are negative. Also keep in mind that P_o and P_i are the water vapor pressure in the chamber and lungs, which are respectively measured and known from the saturation curve.

5.5 Dynamic Flow Model

In this model, some assumptions from our extension of the Drorbaugh and Fenn model are relaxed. In particular, we take into account the flow of air going out through the pneumotacs. This flow is proportional to the pressure difference between the atmosphere and the chamber. Again, the pressure inside the lungs and the pressure in the chamber are assumed to be equal. The inflow of dry air from the left and outflow of chamber-air from the right are also considered to be equal. Thus, we neglect the effect of these two flows on the pressure of air in the chamber. We note that, these flows help maintain the temperature inside the chamber at a constant level.

At time t the parameters in the chamber are denoted as follows:

$P(t)$	The total pressure
P_o^v	The vapor pressure in the chamber
$P_o^d(t)$	The pressure of the dry air in the chamber
T_o	The temperature in the chamber
$V_o(t)$	The volume of the chamber
$n_o(t)$	The total number of molecules in the chamber
$n_o^d(t)$	The number of dry air molecules in the chamber
$n_o^v(t)$	The number of water vapor molecules in the chamber
P_i^v	The vapor pressure in the lungs of the animal
$P_i^d(t)$	The pressure of the dry air in the lungs of the animal
T_i	The temperature of the animal
$V_i(t)$	The volume of the lungs of the animal
$n_i(t)$	The total number of air molecules in the lungs
$n_i^d(t)$	The number of dry air molecules in the lungs
$n_i^v(t)$	The number of water vapor molecules in the lungs

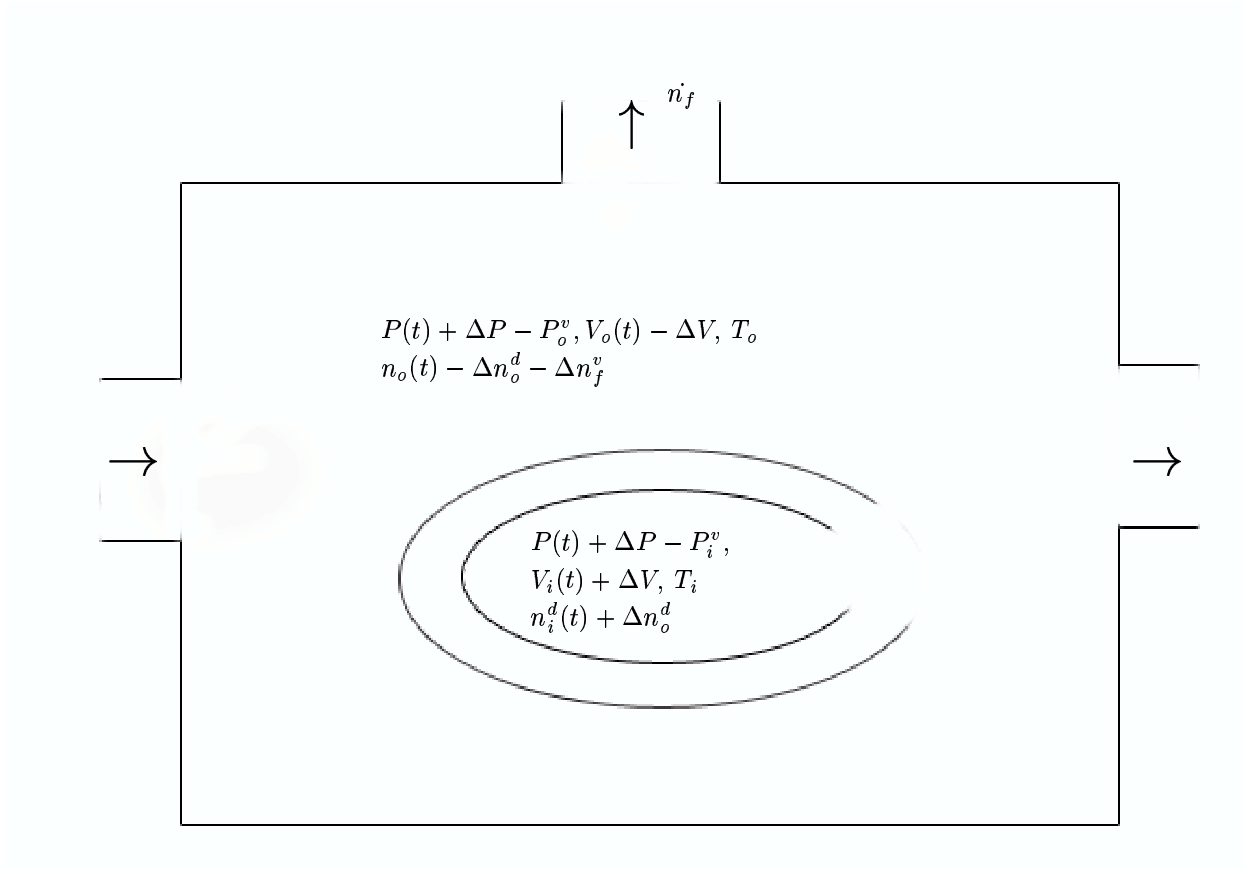

Figure 5.5.1: This is a diagram of the dynamic flow model. $P(t) + \Delta P - P_o^v, V_o(t) - \Delta V$, T_o, and $n_o(t) - \Delta n_o^d - \Delta n_f^v$ represents the pressure, volume, temperature, and dry gas molecules in the chamber, $P(t) + \Delta P - P_i^v, V_i(t) + \Delta V$, T_i, and $n_i^d(t) + \Delta n_o^d$ represents the pressure, volume, temperature, and dry gas molecules in the animal, and $\dot{n_f}$ represents the number of dry air molecules lost through the opening.

The total pressure in the chamber, P, is equal to the total pressure in the lungs at all times.

Let us consider the state of the system during one *inhalation*, that is, at time $t + \Delta t$:

- Δn_o^d is the number of dry air molecules inhaled by the animal.
- The inhalation increases the volume of the lungs by ΔV, thus causing the animal to expand and reduce the effective volume of the chamber by ΔV.
- The volume increase of the lungs increases the pressure in the chamber as well as the pressure in the lungs by ΔP.
- Due to the increase in pressure in the chamber, there is an outflow of some air molecules through the opening at the top of the chamber. Let Δn_f^d denote the number of dry air molecules lost through the opening.
- It is assumed that the chamber has constant exchange of air with the atmosphere, and that the temperature of the air inside the chamber remains constant. Finally, the temperature inside the animal is assumed to remain constant.

Thus, at time $t + \Delta t$, the variables in the chamber are:

$P(t) + \Delta P - P_o^v$	The pressure in the chamber
T_o	The temperature in the chamber
$V_o(t) - \Delta V$	The volume of the chamber
$n_o^d(t) - \Delta n_o^d - \Delta n_f^d$	The number of dry gas molecules in the chamber
$P(t) + \Delta P - P_i^v$	The pressure in the lungs of the animal
T_i	The temperature of the animal
$V_i(t) + \Delta V$	The volume of the lungs of the animal
$n_i^d(t) + \Delta n_o^d$	The number of dry gas molecules in the lungs

Assuming all the movements of the molecules are idealized as quasistatic, the ideal gas law is enforced at all times. Since the total pressure in the chamber and the pressure in the lungs are equal, we obtain (from $PV = nRT$):

$$(P(t) + \Delta P - P_o^v)(V_o(t) - \Delta V) = (n_o^d(t) - \Delta n_o^d - \Delta n_f^d)RT_o \tag{5.5.1}$$

$$(P(t) + \Delta P - P_i^v)(V_i(t) + \Delta V) = (n_i^d(t) + \Delta n_o^d)RT \tag{5.5.2}$$

Equating $P(t) + \Delta P$ in (5.5.1) and (5.5.2):

$$P(t) + \Delta P = \frac{(n_o^d(t) - \Delta n_o^d - \Delta n_f^d)RT_o}{V_o(t) - \Delta V} + P_o^v \tag{5.5.3}$$

$$= \frac{(n_i^d(t) + \Delta n_o^d)RT_i}{V_i(t) + \Delta V} + P_i^v \tag{5.5.4}$$

Equating (5.5.3) and (5.5.4) and neglecting all the second order terms, we obtain:

$$\Delta V[(V_o(t) + V_i(t))P(t) - (P_o^v V_i(t) + P_i^v V_o(t))] - R[(T_o V_i(t) + T_i V_o(t))\Delta n_o^d + T_o V_i(t)\Delta n_f^d] = 0 \tag{5.5.5}$$

We note that the rate of flow of gas molecules through the opening is proportional to the pressure difference between the chamber and the atmosphere. Thus, in a small time Δt,

$$\begin{aligned} \Delta n_f^d &= K_r(P + \Delta P - P_{atm})\Delta t \\ &\approx K_r(P - P_{atm})\Delta t \end{aligned} \tag{5.5.6}$$

Now, the differential form of $P_o^d(t)V_o(t) = n_o^d(t)RT_o$ is:

$$\begin{aligned} \Delta P V_o(t) - \Delta V P_o^d(t) &= -\Delta n_o^d RT_o \\ \Longrightarrow \Delta n_o^d &= \frac{(P(t) - P_o^v)\Delta V - V_o \Delta P}{RT_o} \end{aligned} \tag{5.5.7}$$

Substituting the expressions for Δn_o^d and Δn_f^d from (5.5.6) and (5.5.7) into (5.5.5), we obtain:

$$\dot{V} = F(P(t), V_i(t), V_o(t); T_o, K_r, P_o^v, P_i^v) + G(P(t), V_i(t), V_o(t); T_o, K_r, P_o^v, P_i^v)\dot{P} \tag{5.5.8}$$

where,

$$F(P(t), V_i(t), V_o(t); T_o, K_r, P_o^v, P_i^v) = \frac{T_o V_i(t) R K_r (P(t) - P_{atm})}{(P(t) - P_i^v)V_o(t) - \frac{T_i V_o(t)(P(t) - P_o^v)}{T_o}} \tag{5.5.9}$$

and,

$$G(P(t), V_i(t), V_o(t); T_o, K_r, P_o^v, P_i^v) = \frac{T_o V_i(t) + T_i V_o(t)}{(P(t) - P_i^v)T_o - (P(t) - P_o^v)T_i}. \tag{5.5.10}$$

We assumed that the total pressure in the chamber, P, equals the total pressure in the lungs and that all water vapor pressures are subtracted from the total pressure. We also assumed that the chamber has a constant exchange of air with the atmosphere which implies that the temperature of the air inside the chamber remains constant along with the temperature inside the animal. Finally, by assuming movements of molecules are quasistatic, the ideal gas law is valid in all the conditions. Our model based on these assumptions is shown in Figure 5.5.1.

Equations (5.5.11), (5.5.12), and (5.5.13) are simplified form of equations (5.5.8), (5.5.9), and (5.5.10).

$$\dot{V} = F + G\dot{P} \tag{5.5.11}$$

$$F = \frac{T_o V_i(t) R K_r (P(t) - P_{atm})}{(P(t) - P_i^v) V_o(t) - \frac{T_i V_o(t)(P(t) - P_o^v)}{T_o}} \tag{5.5.12}$$

$$G = \frac{T_o V_i(t) + T_i V_o(t)}{(P(t) - P_i^v) T_o - (P(t) - P_o^v) T_i} \tag{5.5.13}$$

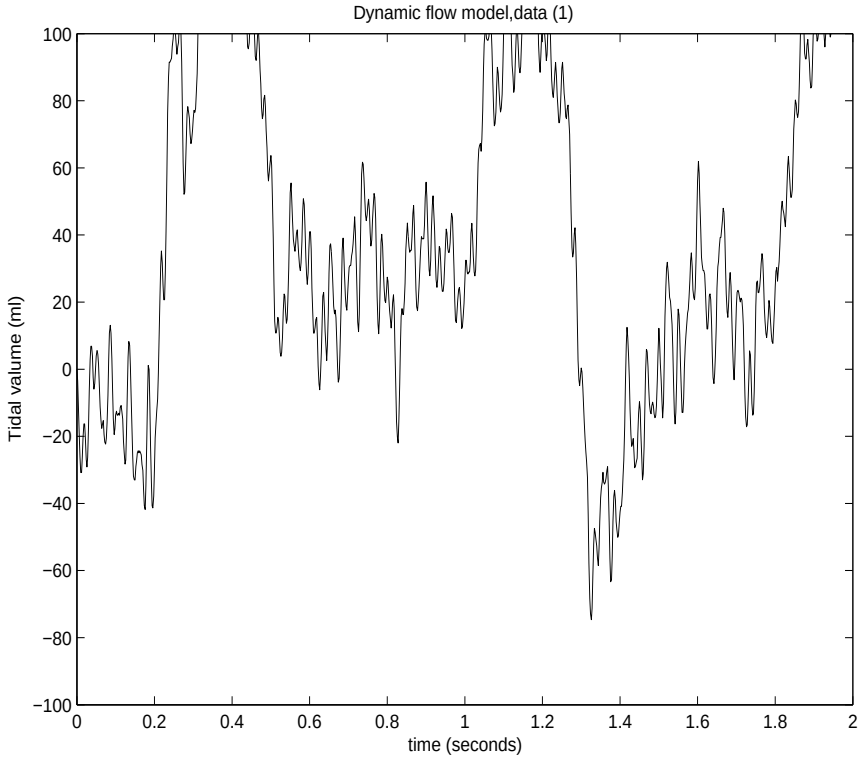

Figure 5.5.2: Dynamic Flow Model (using raw data) with an occupied chamber.

In Figure 5.5.2, when the dynamic flow model is applied to the unfiltered signal the result is not very smooth and shows almost no exhalation, compared to results starting with the filtered signal (see Figure 5.5.3).

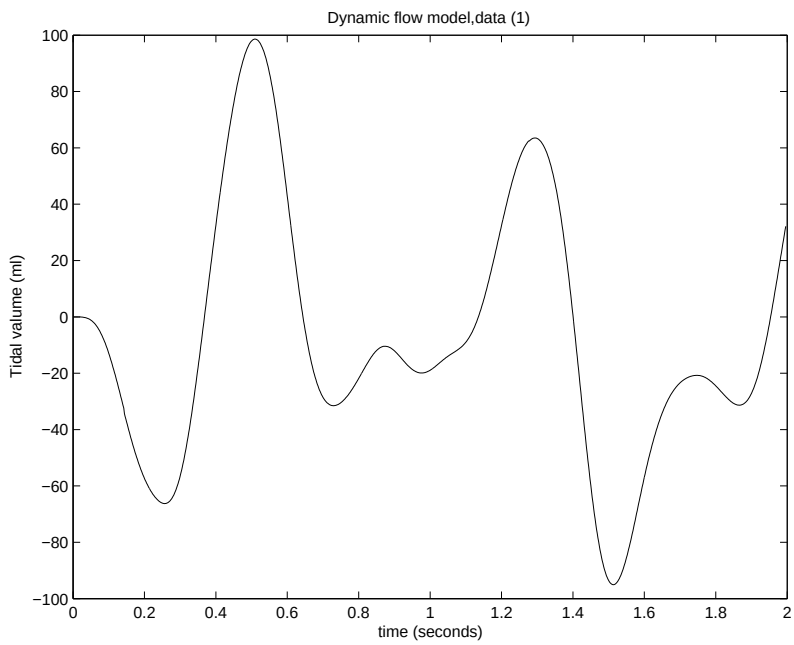

Figure 5.5.3: Dynamic Flow Model (using filtered data) with an occupied chamber.

To derive the dynamic flow model we considered all the inflow and outflow rates and we noted the changes

in internal energies. Temperature changes in the chamber are due to hot and humid exhaled breath and air at a different temperature entering from the left duct. We then found a relationship between $\dot{P}$ and $\dot{V}$ by starting with the ideal gas law, $PV = nRT$, and recognizing that the total volume of air in the chamber does not change as the animal breaths (it is only displaced from outside the animal to inside), though the temperature and pressure do change.

5.5.1 Dynamic Flow Model Extension

Our last task was an extension of the dynamic flow model. This model further generalizes some of the assumptions of the Dynamic Flow Model. Here are some of the main features different from all the above models described:

1. Here we consider all the inflow and outflow rates of air.
2. Our main motivation behind this model is to note the changes in internal energies of the different gas mixtures involved. Thus, we need to consider the temperature changes.
3. Temperature change in the chamber is due to:
   - Hot and humid air being exhaled by the animal.
   - Air entering from the left duct is at a temperature different from that within the chamber.
4. Finally, we intend to get a relationship between $\dot{P}$ and $\dot{V}$.

$$\dot{H}_o = C_{po}(\dot{n}_o^d T_o + n_o^d \dot{T}_o) = \sum_j \dot{n}_j^d H^j(T_j, \frac{P_j^v}{P_j}) \tag{5.5.14}$$
$$\dot{P}V + P\dot{V} = R(\dot{n}_T T_o + n\dot{T}_o)$$

During inhalation

$$\begin{aligned} \dot{n}_T^d &= \dot{n}_{ci} - \dot{n}_o^d - \dot{n}_{co}^d - \dot{n}_f^d \\ \dot{n}_T^v &= -\dot{n}_o^v - \dot{n}_{co}^v - \dot{n}_f^v \end{aligned} \tag{5.5.15}$$

During exhalation

$$\begin{aligned} \dot{n}_T^d &= \dot{n}_{ci} + \dot{n}_o^d - \dot{n}_{co}^d - \dot{n}_f^d \\ \dot{n}_T^v &= \dot{n}_o^v - \dot{n}_{co}^v - \dot{n}_f^v \end{aligned}$$

The derivation of this model is similar to the previous one. We substitute the expression of the rate of change of number of molecules during inhalation from (5.5.15) into (5.5.14) and use the Enthalpy equation to get a relation between $\dot{P}$ and $\dot{V}$. Similarly, we do it for the exhalation cycle.

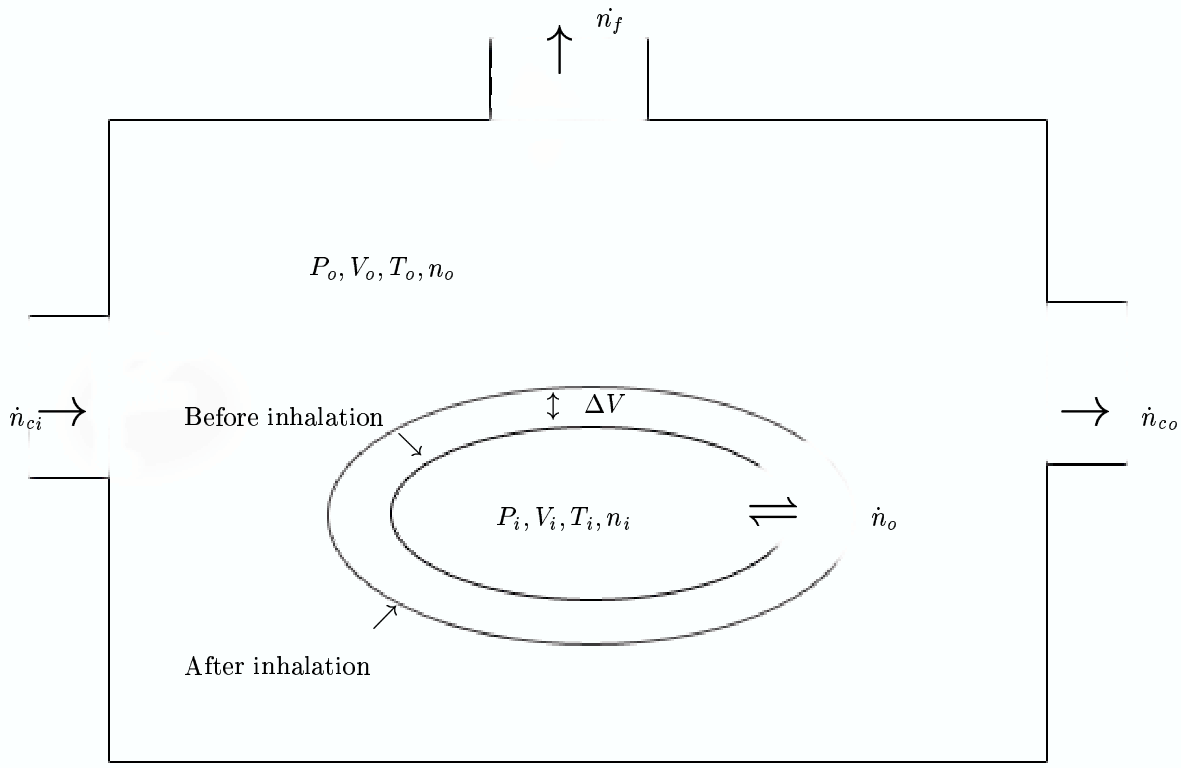

Figure 5.5.4: Dynamic Flow Model (Extension).

5.6 Conclusions and Future Goals

Our results suggest that we could successfully identify acceptable breaths from noisy respiratory data before chlorine exposure provided by CIIT. Features such as a low-pass Butterworth digital filter and criteria to identify good breaths are important steps to accurately calculate the tidal volume. Our filtering method effectively reduced noise from the raw respiratory data. With filter analysis performed both in the time and frequency domains, the high level of noise was significantly minimized after low-pass filtering. In addition, the filtered signal, as compared to the raw signal, more clearly displayed the characteristics expected in respiratory data. With the filtered signal, we could apply the criteria utilized by the "Black Box" to identify good breath signals. We believe our criteria could effectively remove the intermittent noises from various animal movements such as scratching and sniffing. Using our signal processing design, our qualitative evaluations indicate that we can successfully identify acceptable breaths from raw data. However, our signal processing method could not solve the potential problem caused by the persistent mechanical or electrical background interference observed in the empty chamber, which has similar frequency and pattern as the breathing signal. We believe this noise will not have a major effect on our findings since the amplitude of the respiratory signal was significantly higher than the background noise.

We created a dynamic flow model that allows us to readily investigate the questions arising from the Buxco system. To develop our dynamic flow model we first had to start by looking at the currently used Drorbaugh and Fenn model. The dynamic flow model came from an extension of the Drorbaugh and Fenn model where some assumptions were modified. To derive the dynamic flow model we considered all the inflow and outflow rates and noted changes in internal energies. The dynamic flow model, along with filtering the data of an

occupied chamber, allowed us to smooth the data which can be seen in Figures 5.5.2 and 5.5.3. The dynamic flow model also gives us an instantaneous measure of lung volume. In addition to the dynamic flow model, we developed an extension on the dynamic flow model but because of time constraints were unable to apply the extension to the data.

To build on the work presented in this study, we propose future work in three main areas. First, we would like to implement the extension of the dynamic model and observe the improvements, if any. Second, we would also like to observe the effect of chlorine exposure using the dynamic flow model developed. Finally, we would like to investigate how to better handle the potential issues caused by the background noise signal from the unoccupied chamber. We would attempt to identify and minimize any external sources of noise, such as mechanical and electrical interference. In addition, we would like to develop a more sophisticated signal processing method that utilizes the background noise signal from an unoccupied chamber to more effectively reduce the high level of noise from the raw data. One potential method is to measure the background noise signal from an empty chamber, and adjust the noisy respiratory signal of an occupied chamber.

We would like to thank all of the presenters along with Mette Olufsen and Mansoor Haider for all their contributions during the workshop. Our results would not have been possible without them.

Bibliography

[1] A. Adler, J. Bates, C. Irvin, L. Lundblad, : A reevaluation of the validity of unrestrained plethysmography in mice, The American Physiological Society, 2002.

[2] J. Bicudo and J. Chaui-Berlinck, : The signal in total-body plethysmography: errors due to adiabatic-isothermic difference, Elsevier Science, 1998.

[3] CIIT Centers for Health Research, : http://www.ciit.org/, DesignHammer Media Group, LLC, 2004.

[4] J. Drorbaugh and W. Fenn, : A barometric method for measuring ventilation in newborn infants, Pediatrics,16:81, 1955.

[5] M. Epstein and R. Epstien, : A theoretical analysis of the barometric method for measurement of tidal volume, Elsevier/North-Holland Biomedical Press, New York,1977.

[6] R. Epstein, A. Epstien, G. Haddad, and R. Mellins, : Practical implementation of the barometric method for measurement of tidal volume, The American Physiological Society, 1980.

[7] J. Jacky, : Barometric measurement of tidal volume: effects of pattern and nasal temperature, the American Physiological Society, 1980.

[8] M. Kumada, T. Kuwaki, Y. Masuda, and M. Onodera, : Determination of Ventilatory Volume in Mice by Whole Body Plethysmography, Japanese Journal of Physiology Vol.47, No. 4, 1997.

[9] F. Powell and J. Szewcsak, : Open-flow plethysmography with pressure-decay compensation , Elsevier Science, 2002.

[10] P. Schlosser and B. Wong, : Identifying Respiratory Parameters from Plethysmography Data, 2004.

[11] E. Tewksbury, : Buxco Whole Body Plethysomograph Summary, 2004.

[12] H. Trussell, : Signal Processing Frequency Domain Basics Analysis and Filtering, 2004.